DSPACE

https://dspace.org/

Synthesis and characterization of Sm-based orthoferrite compounds, SmFe1-xMnxO3

Usman, Ibrahim Bala

2010-09-07
http://hdl.handle.net/10539/8623

Downloaded from a DSpace repository. https://dspace.org/

SYNTHESIS AND CHARACTERIZATION OF Sm-BASED ORTHOFERRITE COMPOUNDS, $SmFe_{1-x}Mn_xO_3$

IBRAHIM BALA USMAN

SYNTHESIS AND CHARACTERIZATION OF Sm-BASED ORTHOFERRITE COMPOUNDS, $SmFe_{1-x}Mn_xO_3$

IBRAHIM BALA USMAN

A dissertation submitted to the Faculty of Science, University of the Witwatersrand, Johannesburg, in fulfillment of the requirements for the degree of Master of Science.

Johannesburg, 2010

DECLARATION

I declare that this thesis is my own, unaided work. It is being submitted for the degree of Master of Science in the University of the Witwatersrand, Johannesburg. It has not been submitted before for any degree or examination in any other University.

…….

(Ibrahim Bala Usman)

……..day of ……2010

ABSTRACT

The orthoferrites $RFeO_3$ where R is a rare earth and related compounds are being studied because of their important technological applications and unusual magnetic and electrical properties.

Some of these compounds are of interest because of their ferroelectric behaviour as well as for their semiconducting properties. Several elements can be partly or completely substituted for the iron thus providing a means of preparing materials with tailor made properties. These orthoferrites can be antiferromagnetic insulators. The magnetic interactions in such cases are formed as a result of strong negative indirect Fe^{3+}-O-Fe^{3+} interaction. Although these materials are very weak ferromagnetic, they exhibit many properties of ferromagnets. Since the magnetic properties are crucially dependent on both the shape, size of particles and the relative population of the sites or the cation distribution, choosing the right method of preparation becomes crucial. They have wide range of applications in magnetic recording, catalysis, pigments in paints and ceramic among others.

From the previous experiments, there is fairly convincing evidence of $SmFeO_3$ orthoferrite synthesis, albeit with some (5 – 10%) unreacted Fe_2O_3. Unreacted Fe_2O_3 is perhaps an indication of a poorly homogenized sample, and there should be better grinding-mixing procedures.

The substitution of Mn ions in $SmFeO_3$ not only weakens the exchange interaction and reduces the Curie temperature, but also induces a J-T distortion which results in a large electric field gradient at the ^{57}Fe nucleus. During this process the crystallographic structure of the sample is modified by the substitution of Mn ions.

ACKNOWLEDGEMENTS

I am very grateful to my original supervisor Professor G.R. Hearne for introducing me to the field of solid state physics and for the knowledge that I have acquired whilst working with him. I am also thankful for his guidance and patience throughout the project. Dr D. Naidoo (supervisor since July 2009) also deserves my thanks for his help in proof reading my dissertation and guiding me through the submission of my dissertation.

I would like to thank Mr Roy Forbes, Mr Rudolf Erasmus and Dr Emanuela Carleschi for their assistance with the XRD, Raman and Magnetization measurements, respectively.

I am very thankful to Dr Vittoria Pischedda, for her valuable advice and Ms Carol Still for the proof reading of this dissertation.

Finally, I still acknowledge the support, patience and encouragement from my wife *Ramatu* and lovely kids *Usman, Mohammed, Ismail* and *Muhsin*.

DEDICATION

To my parents.

TABLE OF CONTENTS

Declaration ……i

Abstract……..……ii

Acknowledgements..……..iii

Dedication……..iv

Table of Contents ……..v

List of Figures……vii

List of Tables……. x

CHAPTER 1:

Introduction…… ……1

1.1 Background and brief literature review.……2

1.2 Objectives of this research……..……..4

CHAPTER 2:

Description of Techniques…….....5

Introduction……5

2.1 XRD Characterization……5

2.2 Mössbauer Spectroscopy..…….. 10

2.2.1 Resonance Absorption …….. 12

2.2.2 Recoil-free Emission and Absorption...…….....12

2.2.3 Hyperfine Interactions……... 15

2.2.4 Instrumentation…….. 22

2.3 Raman Spectroscopy……..26

2.3.1 The Raman Effect…….. 26

2.3.2 The Classical theory of light scattering…… 28

CHAPTER 3:

Experimental: Sample Preparation and Characterization…….. 31

3.1 Synthesis of $SmFe_{1-x}Mn_xO_3$ Samples…… 31

3.1.1 Procedure for Annealing…… 34

3.2 Sample Characterization...…… 35
3.2.1 Procedure for X-ray Diffraction measurements…….36
3.2.2 Procedure for Mössbauer Spectroscopy measurements.....39
3.2.3 Procedure for Raman Spectroscopy measurements.....45
3.2.4 Magnetization measurements.....48
CHAPTER 4:
Experimental Results and Analysis……... 52
4.1 XRD Crystallograhical properties……..52
4.2 Mössbauer Spectroscopy……... 58
4.3 Raman Spectroscopy……..64
4.3.1 Surface contamination of pelleted samples……64
4.3.2 Raman spectra of all the samples……...66
4.4 Magnetization measurements…….73
CHAPTER 5:
Conclusions……82
REFERENCES…….. 85

LIST OF FIGURES

Fig 1.1 : (a) The unit cell of an "ideal" cubic perovskite structure and (b) The orthorhombic unit cell of $SmFeO_3$……....1

Fig 2.1a : Schematic diagram of an X-ray tube……...6

Fig 2.1b : Diagram of the de-excitation process inside an atom.……....7

Fig 2.1c : Illustration showing the how the Bremsstrahlung radiation is produced....7

Fig 2.2 : Diagram of (220) plane..…….....8

Fig 2.3 : Bragg's law…….9

Fig 2.4 : Nuclear decay of ^{57}Co to ^{57}Fe…….....11

Fig 2.5 : Emission of gamma ray of energy E_γ from an excited state of a nucleus having velocity V…….....13

Fig 2.6 : (a) Isomer shift, δ, is the peak shift from the zero velocity reference and (b) the excited state of ^{57}Fe nucleus with $I = 3/2$ interacts with the asymmetric electronic field, EFG causing quadrupole split; transition from the ground state splits into a doublet, the velocity separation of which is a measure of Δ ……..15

Fig 2.7 : Zeeman splitting of the energy levels in an internal magnetic field and the transitions when $\Delta m_I = 0 \pm 1$…….....20

Fig 2.8 : Spectrum of Fe foil calibration at room temperature where the dots refer to the experimental data ……..22

Fig 2.9 : Schematic diagram of Mössbauer Spectrometer…….....23

Fig 2.10 : Energy level diagrams for Rayleigh and Raman scattering……....27

Fig 3.1 : Mini-pellet press tool...……...32

Fig 3.2 : Hydraulic press...……..33

Fig 3.3 : EUROTHERM 2416 CG Carbolite furnace……35

Fig 3.4 : Zero background sample holder...…….. .36

Fig 3.5 : Schematic diagram of the beam path of Bruker D8 Advance diffractometer.....37

Fig 3.6 : View of the Bruker D8 Advance Diffractometer..……..38
Fig 3.7 : Mössbauer Spectrometer set-up……..41
Fig 3.8 : Cold finger cryostat for low-temperature measurements……42
Fig 3.9 : Schematic diagram of Raman Spectrometer……...44
Fig 3.10 : Raman Spectrometer set-up for room temperature measurements…….46
Fig 3.11 : Diagrammatic representation of the Oxford Instrument Microstat^{He} microscope cryostat used for some of the low temperature measurements…….47
Fig 3.12 : Schematic diagram of a MPMSR. Adapted from L. Fagaly, *Review of Scientific Instruments*, 2006, 101101……..50
Fig 4.1 : The orthorhombic unit cell of $SmFeO_3$……52
Fig 4.2 : XRD spectra of $SmFe_{1-x}Mn_xO_3$ (x = 0, 0.2, 0.5, 0.8 and 1)…….54
Fig 4.3a :XRD pattern of $SmFeO_3$ (x = 0) obtained from experiment and Fig 4.3b : XRD pattern of $SmFeO_3$ (x = 0) from the database (ICSD#=27276)……...55
Fig 4.4a :XRD pattern of $SmMnO_3$ obtained from experiment and Fig 4.4b : XRD pattern of $SmMnO_3$ from the database (ICSD#=95491)…….56
Fig 4.5 : Mn content dependence of the refined orthorhombic lattice constants a, b and $c/\sqrt{2}$. The solid lines indicate trends of the experimental data…...57
Fig 4.6 : Mössbauer spectra of $SmFe_{1-x}Mn_xO_3$ (x = 0, 0.2, 0.5 and 0.8) measured at 293 K……..60
Fig 4.7 : Mössbauer spectra of $SmFe_{1-x}Mn_xO_3$ (x = 0.2, 0.5 and 0.8) measured at 90 K…….61
Fig 4.8 : XRD spectra of $SmFeO_3$ (Pellet and Powder)……65
Fig 4.9 : Raman spectra of the powdered samples of $SmFe_{1-x}Mn_xO_3$ at 293 K……66
Fig 4.10 : Raman spectra of all the non-sintered pellets of $SmFe_{1-x}Mn_xO_3$ at 293 K. ……..67
Fig 4.11 : Raman spectra of all the non-sintered pellets of $SmFe_{1-x}Mn_xO_3$ at 77 K. .68
Fig 4.12 : Raman spectra of $SmFeO_3$ (Powder, Non-sintered and Sintered pellet) at 293 K. The dash lines correspond to 480 cm^{-1} and 610 cm^{-1}.....69

Fig 4.13 : Raman spectra of $SmMnO_3$ (Powder, Non-sintered and Sintered pellet) at 293 K. The dash lines correspond to 480 cm^{-1} and 610 cm^{-1}…..70
Fig 4.14 : Raman Spectrum of $SmMnO_3$ at 293 K…….72
Fig 4.15 : Raman normal modes of $RMnO_3$ in the Pbnm structure (Martin-Carron and de Andres, 2001)…….72
Fig 4.16 : Temperature dependence of magnetization of $SmFe_{0.8}Mn_{0.2}O_3$ in applied field of 50 Oe…… ……....74
Fig 4.17 : Temperature dependence of magnetization of $SmFe_{0.5}Mn_{0.5}O_3$ in applied field of 50 Oe…….74
Fig 4.18 : Temperature dependence of magnetization of $SmFe_{0.2}Mn_{0.8}O_3$ in applied field of 50 Oe……..75
Fig 4.19 : Temperature dependence of magnetization of $SmMnO_3$ in applied field of 50 Oe……...75
Fig 4.20 : Temperature dependence of magnetization of $SmFe_{0.8}Mn_{0.2}O_3$ in applied field of 50 Oe……..... .78
Fig 4.21 : Temperature dependence of magnetization of $SmFe_{0.5}Mn_{0.5}O_3$ in applied field of 50 Oe……..... .78
Fig 4.22 : Temperature dependence of magnetization of $SmMnO_3$ in applied field of 10 Oe……....…….....79
Fig 4.23 : Mn content dependence of Neel Temperature of $SmFe_{1-x}Mn_xO_3$……. .80
Fig 4.24 : Mn content dependence of Transition Temperature of $SmFe_{1-x}Mn_xO_3$… .80
Fig 4.25 : Volume dependence of Neel Temperature of $SmFe_{1-x}Mn_xO_3$……...81

LIST OF TABLES

Table 1 Lattice parameters of $SmFe_{1-x}Mn_xO_3$ (x = 0, 0.2, 0.5, 0.8 and 1)…….....57

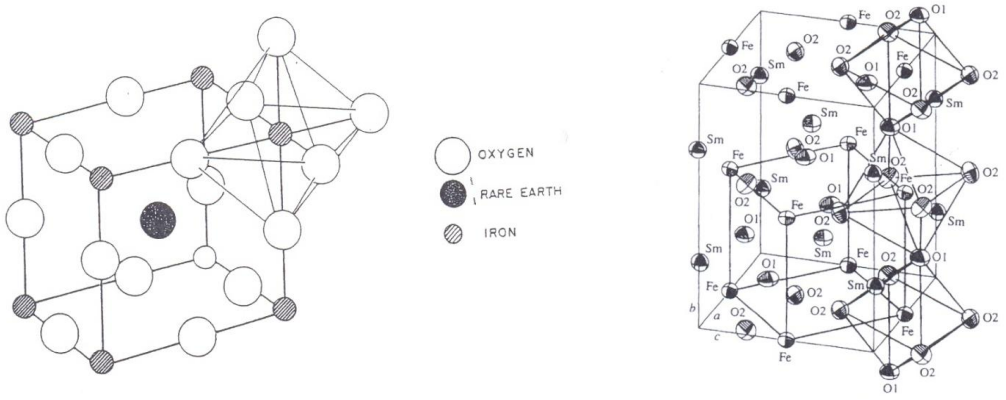
Table 2 Mössbauer parameters of $SmFe_{1-x}Mn_xO_3$ taken at 293 K.....62

Table 3 Mössbauer parameters of $SmFe_{1-x}Mn_xO_3$ taken at 90 K.....62

CHAPTER 1

INTRODUCTION

The orthoferrites $RFeO_3$, where R is a rare earth element, exhibit weak ferromagnetism (Eibschutz et al., 1967). Several elements can be partly or completely substituted for iron (Eibschutz et al., 1967), (Jia et al., 1994), (Li et al., 1998), (Bashkirov et al., 2005), (Rubin et al., 2007), (Nagata et al., 2001), (Porta et al., 2001) to change the structure, properties and potentially create new applications due to the distortion that occurs. These rare earth orthoferrites crystallize in the orthorhombic perovskite structure with the space group *Pbmn*, which is a common arrangement for ABO_3 compounds (Treves, 1965), (Kim et al., 2001). The unit cell of the orthoferrites contains four Fe sites and four rare-earth sites that are cystallographically equivalent (Kim et al., 2001), (Eibschutz et al., 1964). The unit cell of a cubic perovskite structure (Kim et al., 2001) and the unit cell of orthorhombic perovskite structure of $SmFeO_3$ (Maslen et al., 1996) are shown in Fig 1.1(a) and (b) respectively.



(a) (b)

Fig 1.1 : (a) The unit cell of an "ideal" cubic perovskite structure and (b) orthorhombic unit cell of $SmFeO_3$.

1.1 BACKGROUND AND BRIEF LITERATURE REVIEW

The orthoferrites ($RFeO_3$ where R is a rare-earth element) and related compounds have been studied extensively because of their potentially important technological applications and unusual magnetic and electrical properties. The rare-earth orthoferrites are interesting materials for electronic applications because of their mixed conductivity (Stevenson et al., 1996). They display ionic and electronic defects (Cherry M., 1995, Cherry et al., 1995), which makes them important candidates for the development of solid-state fuel cells (Minh, 1993), chemical sensors for the detection of gases [(Carrota et al., 1997), (Carrota et al., 1998)] as well as environmental monitoring applications among others (Martinelli et al., 1999). They belong to the class of strongly correlated electron systems in which the narrow transition-metal (TM) 3d bands and comparatively strong (on-site) Coulomb repulsion U, engender interesting magnetic-electronic properties to this system (Khomskii, 2001), in comparison to the one-electron conventional band-insulator or metal picture of solids. These classes of materials are highly topical in that doped analogs have already "exploded" onto the scene in the new field of "spintronics" (Khomskii and Sawatzky, 1997), (Khomskii, 2001) and as regenerative catalysts (Nishihata et al., 2002). Potential new spintronics materials "multiferroics" have also come into the foreground as a result of new developments whereby magnetization and polarization can coexist in a doped sample (Tokura, 2007).

Mössbauer studies have been carried out on several end members and the doped rare-earth orthoferrites [(Eibschutz et al., 1967), (Jia et al., 1994), (Li et al., 1998), (Bashkirov et al., 2005), (Rubin et al., 2007)]. (Nagata et al., 2001) studied the magnetic properties of $RFe_{1-x}Mn_xO_3$ ($0 \leq x \leq 0.5$) (R = Pr, Gd, Dy) and (Bouziane et al., 2005) of $SmFe_{1-x}Mn_xO_3$ ($0 \leq x \leq 0.3$). They observed that the Mn substituted orthoferrite exhibits a spin reorientation transition from low temperature

antiferromagnetic to high temperature weak ferromagnetic phases. This is as a result of interplay of magnetic-electronic properties between Fe and Mn ions. (Bashkirov et al., 2005) measured the electrical properties (conductivity and activation energy) of $SmFe_xMn_{1-x}O_3$ (x = 0.7, 0.8 0.9) using Mössbauer spectroscopy at room temperature and observed that the conductivity increases and the activation energy decreases with increase in Mn content. (Nagata et al., 2001) found that the resistivity decreases as the content of Mn increases. (Treves, 1965) measured the Curie temperature of $SmFeO_3$ by differential thermal analysis. There have been a number of high-pressure studies recently on the end-member orthoferrites $RFeO_3$, (Rozenberg et al., 2005) and references therein to explore the spin-pairing (high-spin to low-spin) transition and relationship to structural changes. However there has been no high pressure study on $SmFeO_3$, and more importantly no high pressure studies of any of the Mn-doped orthoferrites (i.e. there has been no investigations of the effect of doping on the pressure-induced magnetic-electronic transitions in an orthoferrite).

Structural studies have been carried out on the end members as well (Sangaletti et al., 2001), (Kim et al., 2001), (Maslen et al., 1996) and (Traversa et al., 2000). It has been concluded by (Sangaletti et al., 2001) that the compounds in this family are single phase and that the Fe-O-Fe bond angles shows a monotonic increase with the effective rare-earth (RE) mass. (Kim et al., 2001) observed that the ratio $c/\sqrt{2}a$ for all othorferrites shows a linear dependence on T_N, which implies that the lattice distortion is strongly correlated with the polarizing effect of the RE cation. It has also been concluded that the distortion in the structure of SmFeO3 exhibits either dynamic or static distortion that originates from the bonding characteristics of the RE cations (Maslen et al., 1996). (Traversa et al., 2000) shows that the size of the ions present in the perovskite-type oxides is more important than their chemical nature for the determination of the stable crystalline structure.

Raman studies of the doped and undoped end members have also been carried out by (Martin-Carron et al., 2002). In their analysis of Raman spectra it was concluded that

the stretching modes (symmetric and antisymmetric) correlate to Mn-O bands and the tilt modes to the Mn-O-Mn angle. (Iliev et al., 1998) also concluded that the variations of the lattice distortions affect the phonon frequency as well as the shape of some of the Raman modes. In their work (Alonso et al., 2000) concluded that the steric factor accounts for the increase of the distortion of the perovskite structure as far as the degree of tilting of MnO_6 octahedra is concerned.

1.2 OBJECTIVES OF THIS RESEARCH

The aim of this research is to synthesize and characterize doped $SmFeO_3$ ($RFe_{1-x}Mn_xO_3$ where x = 0, 0.2, 0.5, 0.8 and1) and investigate the impact of Mn on the magnetic-electronic transitions. Mn^{3+} ion is a Jahn-Teller[1] (JT) ion and has the same ionic radius as Fe ($3d^5$) but has a different electronic structure ($3d^4$). The substitution of Mn induces/creates structural modifications. As Mn^{3+} increases it creates a J-T distortion which causes an extension or compression of the Mn^{3+}–O^{2-} bond pairs (local distortion) (Iliev and Abrashev, 2001).

In the work have carried out by (Bouziane et al., 2005) only the iron rich samples of $SmFe_{1-x}Mn_xO_3$ (x = 0.1, 0.2 and 0.3) were investigated. This dissertation is focused on fully characterizing the Mn-rich series as well. It is intended that a high-pressure study will be performed on the samples in future using Fe- Mössbauer spectroscopy, so as to investigate the magnetic-electronic pressure response.

Chapter 2 covers the theoretical description of the techniques used in this dissertation. In chapter 3 the details pertaining to how the experiments were carried out are outlined. Chapter 4 has the experimental results and analyses. Finally chapter 5 covers the conclusion aspects of this dissertation.

[1] Lifting of 3d orbital energy degeneracy by local lattice distortions, and concomitant spatial ordering of occupied 3d orbitals [e_g orbitals for electron configuration $3d^4$ ($t^3{}_2{}_g e^1{}_g$)].

CHAPTER 2

DESCRIPTION OF TECHNIQUES

INTRODUCTION

The following techniques namely X-ray diffraction, Mössbauer Spectroscopy, Raman Spectroscopy and magnetic measurements acquired with MPMS were used for the characterization of the samples ($SmFe_{1-x}Mn_xO_3$ where x = 0, 0.2, 0.5, 0.8 and 1) after they had been synthesized by high a temperature solid state reaction.

(i) X-ray powder diffraction (XRD) was used to identify and characterize the crystal structure of the synthesized composition and to ascertain whether the sample is sufficiently (single) pure phase.

(ii) ^{57}Fe-Mössbauer spectroscopy was used to identify iron bearing constituents and magnetic-electronic characteristics.

(iii) Raman Spectroscopy, for identifying elastic-vibrational behaviour associated with local environment distortions in the material or the onset of structural phase transitions.

(iv) Measurements acquired with MPMS (Magnetic Properties Measurement System) were used to identify the magnetic transition temperatures.

2.1 X-RAY DIFFRACTION CHARACTERIZATION

An X-ray is an electromagnetic wave with high energy (1 – 120 keV), which can be used for structural analysis of materials. Since the wavelengths are comparable to the size of atoms, X-rays are suited for probing the structure of a wide range of materials.

A modern X-ray tube (depicted in Fig 2.1a), designed for crystallographic use, is a permanent evacuated glass envelope into which is sealed a tungsten *filament* separated by about one centimeter from a *target* composed of a metallic element (McKie and McKie, 1992). X-rays are produced in a tube of evacuated glass that contains essentially two electrodes, an anode made of either platinum, tungsten or another heavy metal of high melting point and a cathode. In an X-ray tube, X-rays are generated when a focused electron beam (cathode rays) is accelerated across a high voltage field and bombards a stationary or rotating solid target usually Cu (with a wavelength of 1.5418Å for the K radiation). When electrons move from ground state to a higher state, they become "excited" and "de-excited" when they move from ground to a lower state. This is illustrated in Fig 2.1b. As the electrons collide with atoms in the target and slow down, a continuous spectrum of X-rays are emitted, which are termed Bremsstrahlung radiation (see Fig 2.1c). Through an ionization process, the high energy electrons also eject inner shell electrons in the atoms. When a free electron fills the shell, a photon of X-ray with energy characteristic of the target material is emitted.

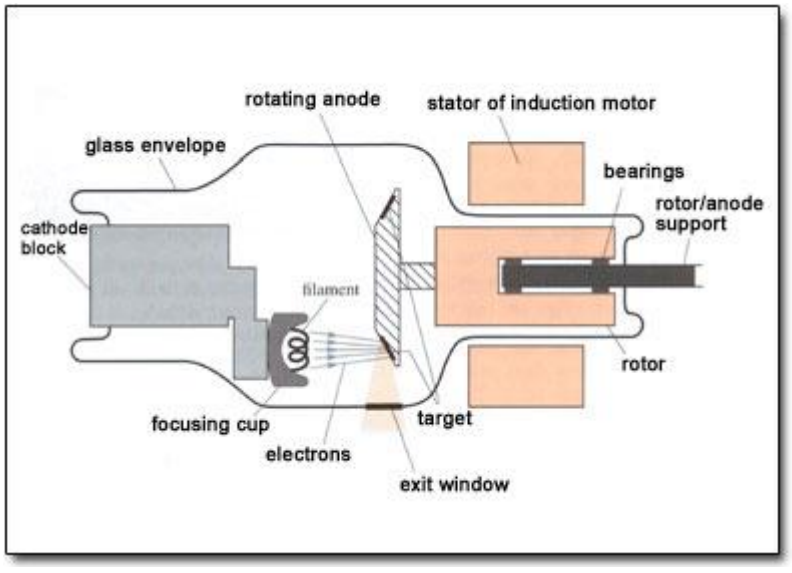


Fig 2.1a : Schematic diagram of an X-ray tube.

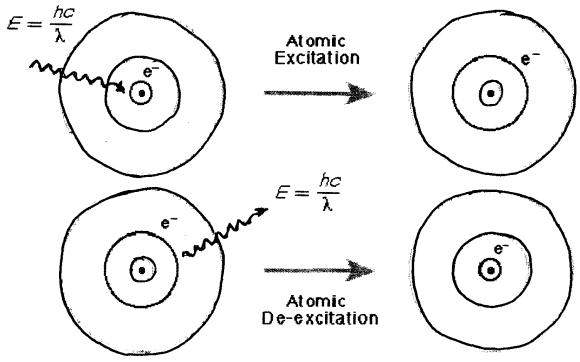


Fig 2.1b : Diagram of the de-excitation process inside an atom.

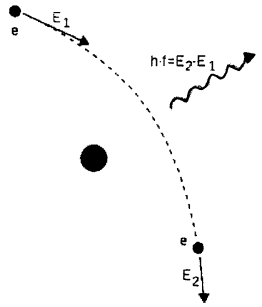


Fig 2.1c : Illustation of how the Bremsstrahlung radiation is produced.

An electron in an alternating electromagnetic field will oscillate with the same frequency as the field. When an X-ray beam hits an atom, the electrons around the atom start to oscillate with the same frequency as the incoming beam. In almost all directions we will have destructive interference, that is, the combining waves are out of phase and there is no resultant energy leaving the solid sample. Since the atoms in a crystal are arranged in a regular pattern, and in very few directions as defined by the planes in which the atoms are located we will have constructive interference. The waves will be in phase and there will be well defined X-ray beams leaving the sample in various directions. Hence, a diffracted beam may be described as a beam composed of a large number of scattered rays mutually reinforcing one another. The most useful information is obtained when the material is crystalline.

This model is complex to handle mathematically, and in day to day work we talk about X-ray reflections from a series of parallel planes inside the crystal. A plane passing through three non-colinear lattice points is known as a *lattice plane* (McKie and McKie, 1992). Any family of planes may be identified by integers called *Miller indices.* The Miller indices named (*hkl*) are reciprocals of the fractional coordinates of the axial intercepts of the first plane away from the origin. A given set of planes with indices (*hkl*) cut the *a*-axis of the unit cell in *h* sections, the *b* axis in *k* sections and the c-axis in *l* sections. A zero indicates that the planes are parallel to the corresponding axis, e.g. the (220) planes cut the *a*– and the *b*– axes in half, but are parallel to the *c*– axis shown in Fig 2.2.

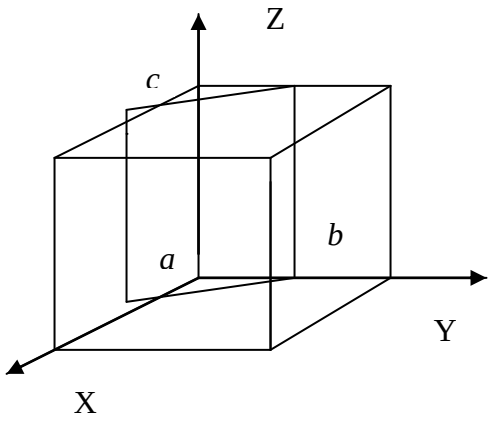


Fig 2.2 : Diagram of (220) plane.

In powder or polycrystalline diffraction it is important to have a sample with a smooth plane surface. If possible, we normally grind the sample down to particles of about 0.002 mm to 0.005 mm in cross section. The ideal sample is homogeneous and the crystallites are randomly distributed. The sample is side loaded into a sample holder so that we have a smooth flat surface.

Ideally we now have a random distribution of all possible (*hkl*) planes. Only crystallites having reflecting planes (*hkl*) parallel to the specimen surface will

contribute to the reflected intensities. If we have a truly random sample, each possible reflection from a given set of (*hkl*) planes will have an equal number of crystallites contributing to it. We only have to rock the sample through the glancing angle θ in order to produce all possible reflections.

Lattice Planes and Bragg's Law

When X-ray photons collide with electrons, some photons from the incident beam will be deflected away from their original path. If the wavelength of the scattered X-rays did not change (i.e the photons did not lose any energy), the process is then called elastic scattering in that only momentum has been transferred in the process.

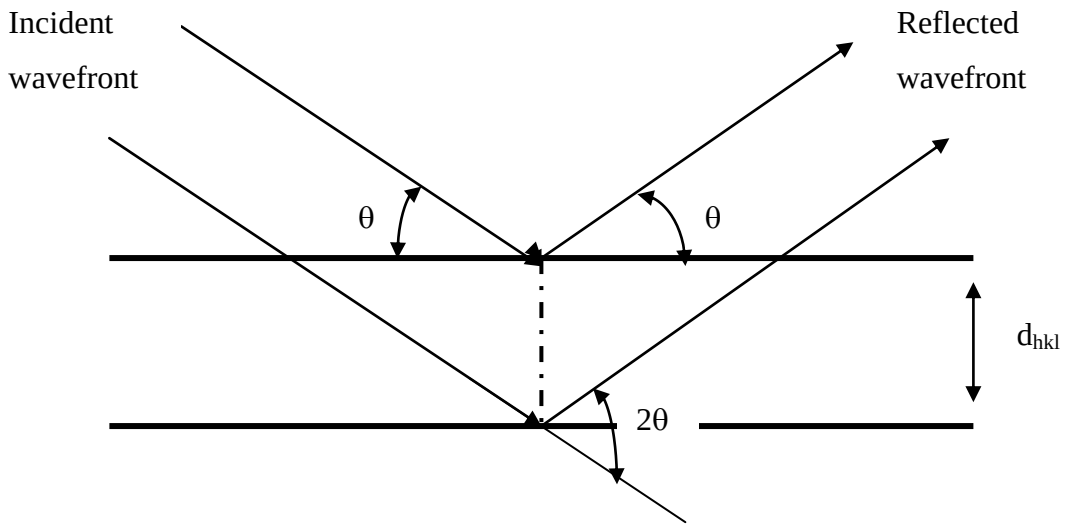


Fig 2.3 : Bragg's law.

X-ray diffraction (XRD) is a non-destructive technique that reveals information about the crystallographic structure, chemical composition and physical properties of materials. The peaks in an X-ray diffraction pattern are directly related to the atomic distances. For a given set of lattice planes with an inter-plane distance of d, the

scattered waves undergo constructive interference i.e. the waves remain in phase since the path length of each wave is equal to an integer multiple of the wavelength. That is the condition for a diffraction (peak) to occur follows Bragg's law.

$$2d_{hkl} \sin\theta = n\lambda$$

where θ is the scattering angle, n is an integer, d_{hkl} is the spacing between the lattice planes and λ the wavelength of the X-ray as shown in Fig 2.2. Very strong intensities known as Bragg peaks are obtained in the diffraction pattern when scattered waves satisfy the Bragg condition.

2.2 MÖSSBAUER SPECTROSCOPY

The Mössbauer Effect (ME) is the emission or resonance absorption of gamma-ray photons without loss of energy due to recoil and without thermal broadening. This effect was discovered by Rudolf L. Mössbauer in 1957 whilst studying resonance absorption of γ-rays in ^{191}Ir.

The most commonly used isotope in Mössbauer Spectroscopy (MS) is ^{57}Fe followed by ^{119}Sn. For ^{57}Fe Mössbauer Spectroscopy, radioactive ^{57}Co which has a half-life of 270 days, decays by electron capture to the I = ⅝ excited state of ^{57}Fe which subsequently decays to the I = ¾ state. ^{57}Fe decays to its ground state by emitting the 14.4 keV γ-ray required for MS. The decay process is depicted in Fig 2.4.

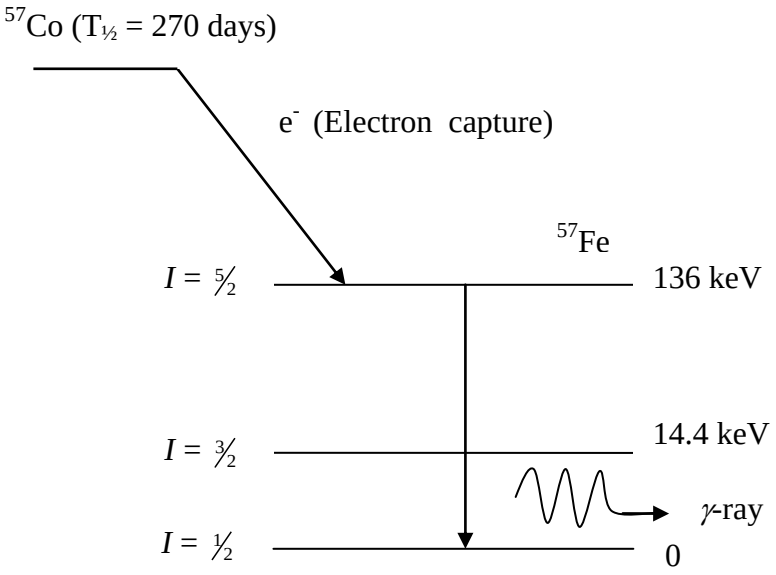


Fig 2.4 : Nuclear decay of ^{57}Co to ^{57}Fe.

Mössbauer transitions have been observed in about 70 isotopes and about 40 elements. Mössbauer Spectroscopy has many applications and a few are listed below;

i. Characterization of the oxidation states of iron (Fe^{2+}, Fe^{3+}).
ii. Co-ordination position of iron atoms (octahedral, tetrahedral, planar) and nature of the distortion of the site symmetry.
iii. Structural variations, identified from magnetic properties.
iv. Oxidation of minerals.

2.2.1 RESONANCE ABSORPTION

In spectroscopy, the γ-rays emitted from a radioactive nucleus is modulated by inducing a Doppler velocity to the source, and the γ-rays of discrete energies are resonantly absorbed by absorber nuclei.

2.2.2 RECOIL-FREE EMISSION AND ABSORPTION

Consider a nucleus of mass M in an excited state E_{ex} which undergoes a transition to the ground state of energy E_{gr}. A quantum of energy $E_t = E_{ex} - E_{gr}$ in the form of a γ-ray is emitted during this transition. Let M be the mass of the nucleus and E_{gr} and E_{ex}, the ground and excited states energies, respectively. These states are separated by an energy of transition E_t and a γ-ray of energy E_γ is emitted as shown in the equation Fig 2.5.

If an excited atom is initially moving with a velocity V in the direction of emission of the γ-ray, its total energy above the ground state (at rest) is $E_{ex} + \frac{1}{2}MV^2$. If the nucleus recoils due to the γ-ray emission it attains a new velocity $V + v$ and a kinetic energy given by $\frac{1}{2}M(V+v)^2$. The law of conservation of energy demands the following:

$$E_{ex} + \tfrac{1}{2}MV^2 = E_{gr} + E_\gamma + \tfrac{1}{2}M(V+v)^2 \qquad (2.1)$$

$$\therefore E_\gamma = E_{ex} - E_{gr} - \tfrac{1}{2}Mv^2 - MVv \qquad (2.2)$$

$$\therefore E_t - E_\gamma = \tfrac{1}{2}Mv^2 + MVv = E_R + E_D \qquad (2.3)$$

The term, $\frac{1}{2}Mv^2$, is called the recoil energy, E_R, which is independent of the initial velocity, V, of the excited nucleus. The other term MVv, is the Doppler or thermal energy, and is denoted by E_D.

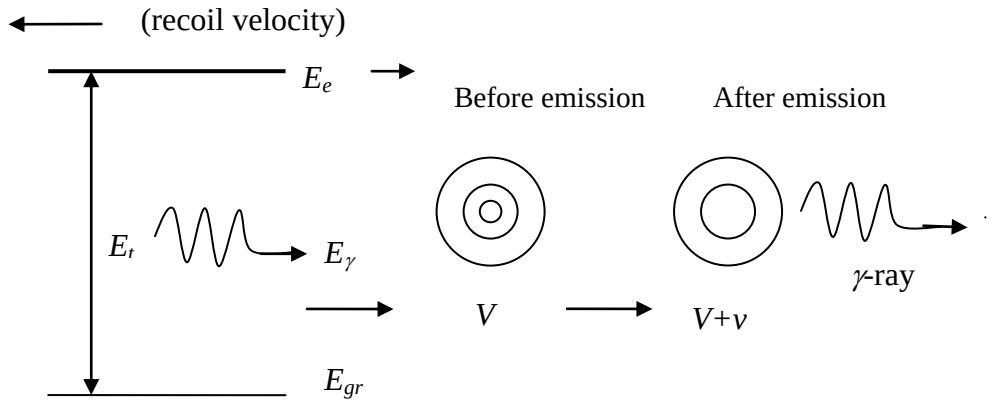


Fig 2.5 : Emission of gamma ray of energy E_γ from an excited state of a nucleus having velocity V.

The equation (2.3) now becomes

$$E_\gamma = E_t - E_R - E_D \qquad (2.4)$$

By employing the principle of conservation of momentum, we have

$$MV = M(V+v) + E_\gamma / c\,,$$

where E_γ / c is the momentum of the γ-ray photon and c is the velocity of light. Simplifying the above equation gives

$$E_\gamma / c = -Mv \qquad (2.5)$$

For ^{57}Fe, the Mössbauer transition between the first excited state and the ground state (E_γ = 14.4 keV) results in $E_R = 1.95 \times 10^{-3}$ eV. This energy comparable to when a bullet leaves a gun, is of the order of 10^{-2} to 10^{-3} eV, and is

$$E_R = E_\gamma{}^2 / 2Mc^2 \qquad (2.6)$$

The emitted gamma rays have energies of 10–100 keV.

The Doppler energy (E_D) in equation 2.4 implies that the energy of the γ-ray, emitted in the direction of the movement of the nucleus, differs from the energies of γ-rays emitted in other directions. The distribution of energies resulting from the translational motion of the source nuclei in many directions causes ***Doppler broadening*** of the energy distribution. Therefore the Doppler energy becomes

$$E_D = 2(E_R / kT)^{\frac{1}{2}} = E_\gamma (2kT / Mc^2)^{\frac{1}{2}}$$

where k is the Boltzmann constant and T the temperature,

$$\therefore E_t - E_\gamma = E_\gamma{}^2 / 2Mc^2 + E_\gamma (2kT / Mc^2)^{\frac{1}{2}} = E_R + E_D$$

It is the recoil energy that destroys the resonance condition. The strength of the resonant absorption is determined by the overlap of the energy profiles for the source and absorber.

When the source and absorber atoms are in different local environments, their nuclear energy levels are different as shown in Fig. 2.6. The ½ and ³⁄₂ labels represent the nuclear spin, or intrinsic angular moment, quantum numbers, I.

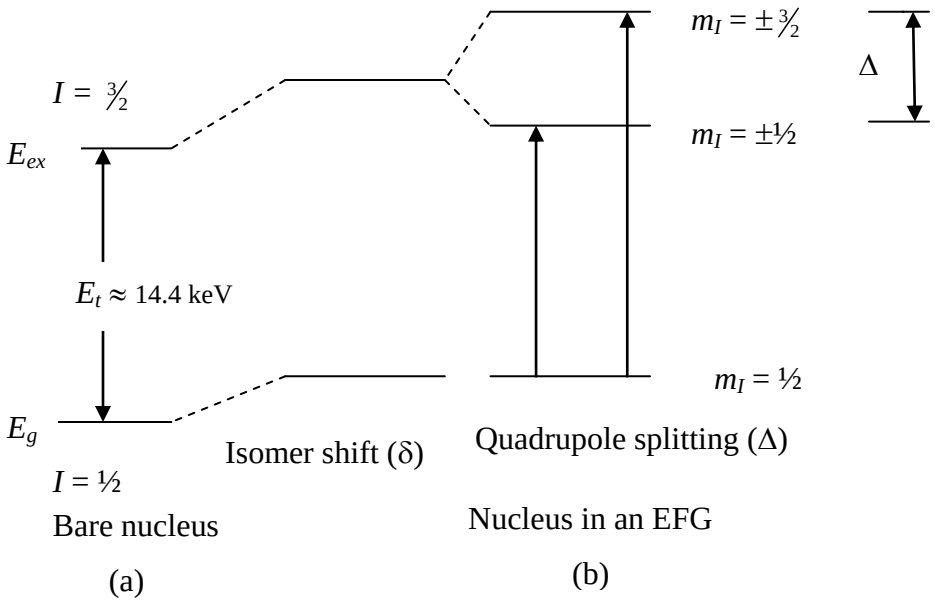


Fig 2.6 : (a) Isomer shift, δ, is the peak shift from the zero velocity reference and (b) the excited state of ^{57}Fe nucleus Δ with $I = 3/2$ interacts with the asymmetric electronic field, EFG causing quadrupole split; transition from the ground state splits into a doublet, the velocity separation of which is a measure of Δ.

2.2.3 HYPERFINE INTERACTIONS

The energy of a nucleus is influenced by the chemical environment of its atom. The Hamiltonian equation describing the energy of the nucleus is written as:

$$H = H_O + E_{CS} + M_{hf} + E_{efg}$$

where

H_o = all terms excluding the hyperfine interactions with the environment.

E_{cs} = *Chemical or Isomer shift*, which is caused by the interaction with the electrons. This causes a line shift.

M_{hf} = *Magnetic hyperfine* splitting term, describing the effect of the interaction of the

nuclear spin with the magnetic field splitting.

E_{efg} = *Electric quadrupole interaction* term, describing the interaction of the nuclear quadrupole moment with the local *electric field gradient* (EFG) produced by the surrounding charge distribution. This also causes line splitting.

spectra are described using three parameters namely isomer shift (δ), which arises from the difference in *s* electron density at the nuclear site between the source and the absorber, quadrupole splitting (Δ) which is a shift in nuclear energy levels that is induced by an electric field gradient (EFG) interacting with the quadrupole moment caused by the nearby electrons, and the magnetic hyperfine splitting (Bhf) (arising from magnetic moment interacting with internal magnetic field) for magnetic materials only.

i. ISOMER SHIFT

Resonance absorption occurs when the emitter ^{57}Co and the absorber ^{57}Fe are in the same matrix. The difference in energies is called chemical shift or isomer shift, denoted by δ which arises due to the difference in *s*-electron density at the nuclei of radioactive source and the absorbing iron nuclei in the sample or absorber. Isomer shift represents the electric monopole interaction involving the positive nuclear charge and the electric field of surrounding electrons. This interaction causes a shift of the energy levels with respect to the bare nucleus. Isomer shift (δ) is affected by oxidation state, coordination number, the spin state of iron atoms and the second order Doppler shift, which is temperature dependent. The isomer shift depends heavily on a calibration standard, which are α-Fe foil, stainless steel or α-Fe_2O_3 in which the mid-point of the individual spectrum is measured for zero velocity position.

ii. QUADRUPOLE INTERACTION

If the spin quantum number (I) is 1 or greater ($I \geq 1$), the nuclei will have a quadrupole moment, eQ, which may interact with the surrounding electric field gradient (EFG). The excited state of ^{57}Fe ($I = 3/2$) has a quadrupole moment. In the presence of a non-spherically symmetrical electric field the excited state having non-spherical (elliptical) charge distribution assumes different orientations in relation to the field, and the energy levels split. This is called quadrupole splitting, the magnitude of which is equal to $\frac{1}{2}e^2qQ$, where e is the electron charge, q is the gradient of the electrostatic field at the nucleus, and Q is the nuclear quadrupole moment. Transition to these substate levels from the ground state gives a two-line pattern as shown in Fig 2.6. The velocity difference between the lines is a measure of the quadrupole splitting (QS).

Quadrupole splitting of Fe^{3+} is a measure of degree of distortion of Fe^{3+}–O polyhedral, which increases with increasing Z/r^3 of the metal cation. The quadrupole splitting is determined by the charge state and by the local environment of the ion.

ELECTRIC FIELD GRADIENT

The electric field (E) at the nucleus is the negative gradient of potential:

$$E = -\nabla V$$

where ∇ is the grad operator. One can write

$$V_y = \frac{\delta^2 V}{\delta_i \delta_j}.$$

Hence, the *EFG* can be written as

$$EFG = -\begin{bmatrix} V_{xx} & V_{xy} & V_{xz} \\ V_{yx} & V_{yy} & V_{yz} \\ V_{zx} & V_{zy} & V_{zz} \end{bmatrix}$$

Of the nine components of the EFG tensor, only five may be considered to be independent parameters (May, 1971). Three of the off-diagonal elements are dependent since $V_{xx} = V_{yx}$, etc., and one of the diagonal elements is dependent because Laplace's equation

$$V_{xx} + V_{yy} + V_{zz} = 0$$

must be satisfied.

The values of the EFG tensor elements depend on the choice of the coordinate axes. This coordinate system is the one for which the off-diagonal elements are zero and the diagonal elements are ordered such that

$$|V_{xx}| > |V_{yy}| > |V_{zz}|$$

Evidently two of these are independent and V_{zz} is proportional to QS and is used for defining $\eta = (V_{xx} - V_{yy})/V_{zz}$ where η is the asymmetry parameter $(1 > \eta > 0)$. V_{zz} is equal to the *Z* component of the EFG and also equal to *eq*, where *e* is the proton charge. The EFG can be specified by the two parameters V_{zz} and η. There are two sources which contribute to the EFG namely;

i. the surrounding lattice and
ii. electronic configuration of ion.

For $I = 3/2$ (in ^{57}Fe) the relationship between QS, Q, V_{zz} and η is represented as:

$$QS = \frac{-e}{2} V_{zz} Q \sqrt{\left(1 + \frac{\eta^2}{3}\right)} = \frac{e^2}{2} qQ \sqrt{\left(1 + \frac{\eta^2}{3}\right)}$$

where $eq = V_{zz}$ = Z-component of EFG and Q is the quadrupole moment of the nucleus.

iii. MAGNETIC HYPERFINE INTERACTION

In the presence of a magnetic field the nuclear spin moment experiences a dipolar interaction with the magnetic field called the Zeeman splitting. There are many sources of magnetic fields that can be experienced by the nucleus.

A nucleus having a spin I possess a dipole moment U_N, given by,

$$U_N = g_N \mu_N I$$

where g_N = nuclear Lande g factor. U_N = nuclear Bohr magneton which is equal to $e\hbar/2mc$, where e and m are the charge and mass of the proton, and c is the speed of light. The magnetic dipole moment U_N, interacts with the local or applied fields at the nucleus, thereby removing the degeneracy of the nuclear and energy levels completely as shown in Fig 2.7.

There are various sources contributing to the effective magnetic field (Gutlich et al., 1978), the most important of which are

i. The Fermi contact field, which arises from a net spin (up or down) of the *s*-electron density at the nucleus;

ii. A contribution from the orbital motion of the valence electrons and

iii. Spin-dipolar field contribution arising from the electron spin of the atom under consideration.

iv.

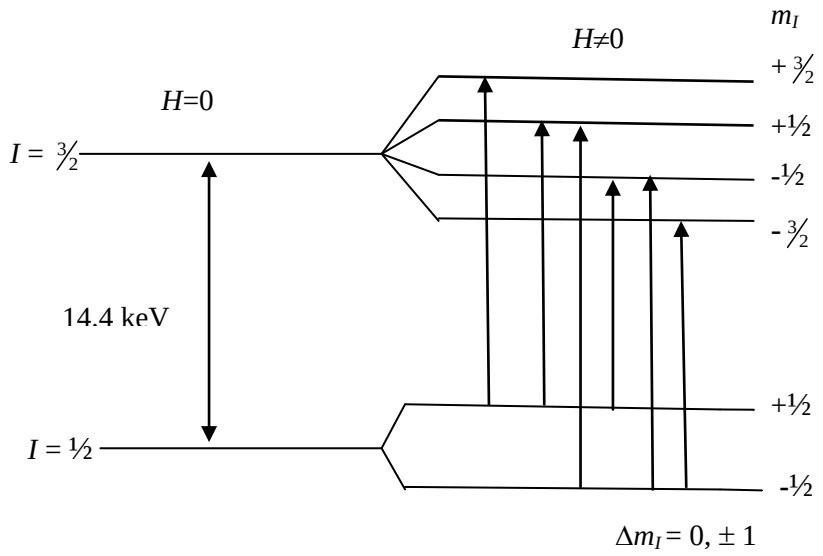


Fig 2.7 : Zeeman splitting of the energy levels in an internal magnetic field and the transitions when $\Delta m_I = 0 \pm 1$.

For ^{57}Fe, the selection rules $\Delta m_I = 0, \pm 1$ gives a symmetrical six-line spectrum. The line-widths Γ, of the peaks are similar but the intensities differ. The relative intensities of the six-lines is 3:2:1:1:2:3.

iv. COMBINED HYPERFINE INTERACTIONS

The electric quadrupole interaction describes the interaction of the nuclear quadrupole moment *Q* (a property of the nucleus) with the local electric field gradient (a property of the sample) produced by the surrounding charge distribution. In the

presence of a magnetic field the nuclear spin moment experiences a dipolar interaction with the magnetic field i.e. Zeeman splitting. Figure 2.8 shows a spectrum indicating hyperfine interaction.

If there is a combined electric and magnetic hyperfine interaction then an asymmetric magnetically split Mossbauer spectrum is produced. If $V_{zz} > 0$ an asymmetric magnetic split is the case and the quadrupole shift now becomes a function of an angle.

$$QS = \frac{e^2 qQ}{8}(3\cos^2\theta - 1)$$

where θ is the angle between V_{zz} and the magnetic field,

eQ is nuclear constant for the resonant isotope and

eq $(3\cos^2\theta - 1)$ = V_{zz} is electric field gradient (EFG).

There are many sources of magnetic fields that can be experienced by the nucleus. There are two sources which contribute to the EFG namely;

i. the surrounding lattice and
ii. the electronic configuration of the ion.

The angular dependence of the quadrupole splitting causes orientation of the spins in the structure.

For non magnetic field,

$$QS = \frac{e^2 qQ}{2}.$$

Fig 2.8 shows a typical spectrum of α-Fe used for calibration purposes (see Chapter 3).

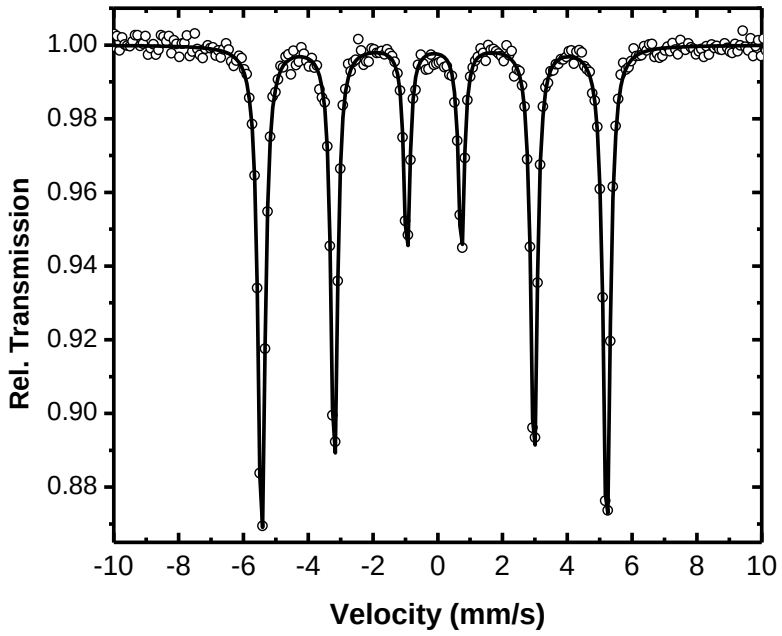


Fig 2.8 : Spectrum of α-Fe foil at room temperature where the dots refer to the experimental data and the solid lines represents a theoretical fit.

2.2.4 INSTRUMENTATION

An experimental setup consists of a radioactive source (^{57}Co), a drive mechanism for producing a Doppler velocity, a gamma-ray detector with amplifying and sorting attachment followed by a data sorting device such as a multi-channel analyzer. The spectrum is a record of the transmission rate of the resonant γ-rate, as a function of Doppler velocity between the source and the absorber. By mounting the source on a mechanical *constant-velocity* drive the total number of counts can be registered in a *fixed time*, at constant velocity, and subsequently re-measured at different velocities. The *multi-channel analyzer* (MCA) employed as data-storage, is *synchronized with*

vibrator sweeps. A square wave from the multi-channel analyzer with leading edges at channels 0 and 200 is integrated to give a systematic triangular signal.

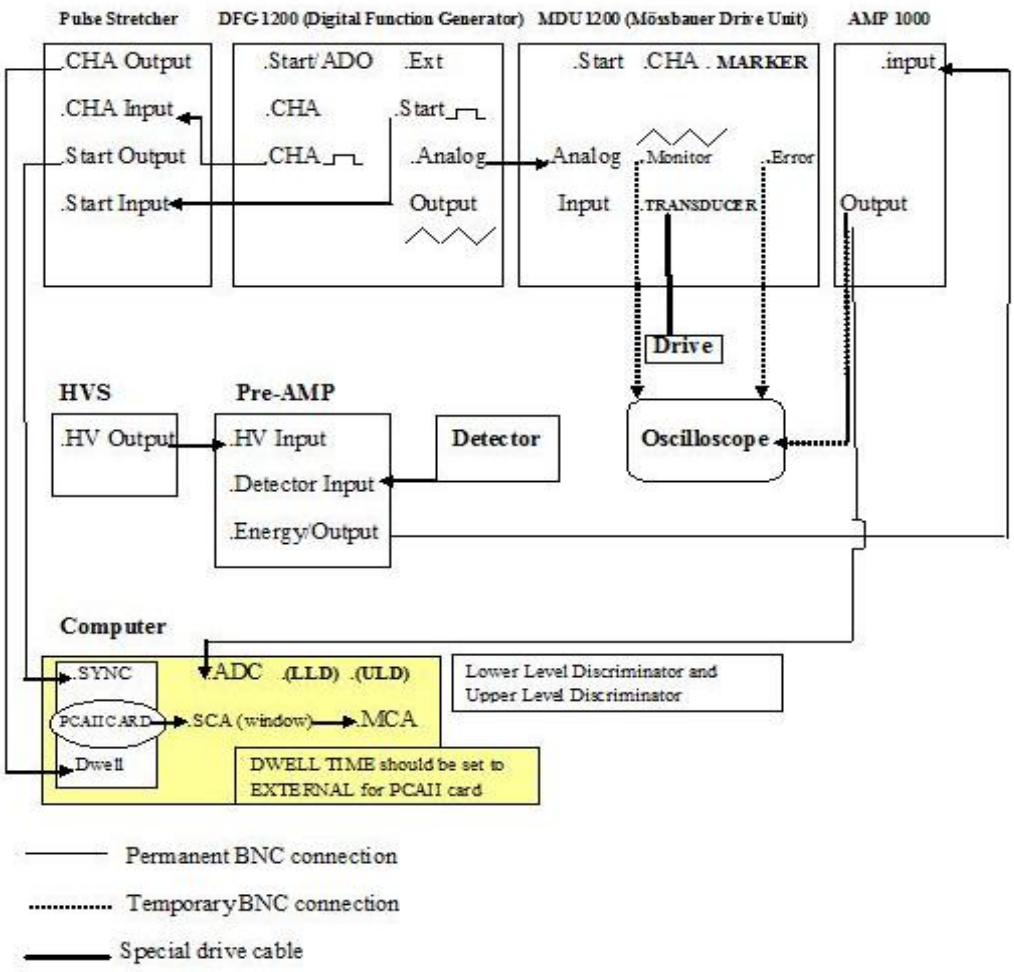


Fig 2.9 : Schematic diagram of Spectrometer.

The functions of the various electronic modules are listed below;

- Detector - for detecting gamma-rays with amplifying and sorting attachment;
- Drive - The velocity and analyser sweeps are synchronized and gamma rays from a given velocity are always fed to the same channel analyser;

- Multi-channel analyser (MCA) - employed as data storage;
- Pre-Amplifier – for converting the small charge pulse from the detector to a larger pulse;
- Amplifier (AMP) – it produces amplification (50 – 2000 times) and shaping the pulses so that they are suitable for analysis by a single channel analyser;
- Single channel analyser (SCA) – serves as a discriminator (it selects pulses from the 14.4 keV gamma rays and reject those outside this region).

Source (the host of ^{57}Co–^{57}Fe)

A source should give the narrowest possible Lorentzian lines. For this to be achieved, the following conditions are pre-requisites:

- The host material should be *chemically inert* i.e. not susceptible to oxidation.
- The source atoms are located in a cubic matrix made of Rhodium.
- The source atoms should have a *maximum f factor*, which is possible only in metallic or ionic lattices.
- The host matrix should not generate X-rays or Compton scattering.

Preparation and optimum thickness of the absorber

Most absorbers used in spectroscopy are in the range of 20 – 200 mg with the size being inversely proportional to the iron concentration within the sample. Powder samples must be crushed finely enough that they present a uniform appearance to the gamma-ray beam. If the sample has a high iron concentration, so that its optimum thickness is small, then it has to be mixed with an extender in order to achieve a uniform loading across the absorber holder. The most common extenders white sugar, powdered milk, boron nitride and boric acid. The following have to be taken into account when choosing the optimum sample thickness (Murad and Cashion, 2004);

1. There should be sufficient resonant nuclei to obtain a reasonable dip and the dependence is linear for small concentrations.
2. If the sample is too thick with resonant nuclei, there will be appreciable line broadening.
3. If the sample is too thick with non-resonant nuclei, then electronic absorption will reduce the count rate to unacceptable low values.

Usually we optimize for the following among others;

(i) best resolution for hyperfine interactions,
(ii) best signal to noise ratio and
(iii) minimum counting rate.

An absorber should be as thin as possible. An optimal sample concentration of 5 to 7 mg of Fe/cm^2 is desirable. The mass absorption coefficients, μ_e/ρ (μ_e is the absorption coefficient and ρ is the density of the absorber), are given as a function of wavelength has been tabulated at 14.4 keV for all elements by (Long et al., 1983). The mass absorption coefficient for the total absorber, $(\mu_e/\rho)_{tot}$, is given by

$$(\mu_e/\rho)_{tot} = \sum f_i(\mu_e/\rho)_i$$

where f_i is the mass fraction of the i^{th} element. For most absorbers, the optimum thickness will be approximately $1/[(\mu_e/\rho)_{tot}]$. This gives the optimum as an area thickness with units of g/cm^2. The most common absorbers used for calibration are α-Fe, hematite and stainless steel.

Detectors

^{57}Fe spectroscopy is usually done using a gas-filled proportional detector, for example Kr or Kr-CO_2 which has a good efficiency at 14.4 keV.

2.3 RAMAN SPECTROSCOPY

2.3.1 The Raman Effect

Raman spectroscopy is concerned with the phenomenon of a change of frequency when light is scattered by molecules. If the frequency of the incident light is ν_o and that of the scattered light is ν_r, then the frequency shift $\nu_r - \nu_o = \Delta\nu$ may be either positive or negative in sign. Its magnitude is referred to as a Raman frequency. The set of Raman frequencies of scattering species constitutes its Raman spectrum. A frequency shift is equivalent to an energy change $\Delta\nu/h$.

When monochromatic light of frequency ν_o is used, the spectrum of the scattered light shows (in addition to the Rayleigh line) a pattern of lines of shifted frequency – the Raman spectrum. The shifts (Raman frequencies) are independent of the exciting frequency ν_o and are characteristic of the species giving rise to the scattering.

Photons are absorbed by materials and are scattered when a beam of light is incident on a sample. On collision with a molecule, a photon may be elastically scattered i.e. without change in energy. This gives rise to the Rayleigh line. Collisions may however be inelastic. They may cause the molecule to undergo a quantum transition to a higher energy level, with the result that the photon loses energy and is scattered with lower frequency ($\Delta\nu$ negative). The Raman shifts are equivalent to the energy changes involved in transitions of the scattering species and are therefore

characteristic of it. The Raman shifts correspond to vibrational or rotational transitions of the scattering molecule.

Most of the scattered photons have the same wavelength as the incident photons and are known as *Rayleigh scattered* light while the rest are shifted to a different wavelength (*Raman scattering*). Most of the Raman scattered photons are shifted to a longer wavelength (*Stokes shif*t), but a small portion are shifted to a shorter wavelength (*anti-Stokes shift*).

The Raman effect is also applicable to crystals not just molecules. In the case of crystals the energy absorption/emission related to the Raman effect concerns the vibrational energy levels in a crystal. Energy level diagrams for Rayleigh and Raman scattering are shown in Fig 2.10 (Long, 2002).

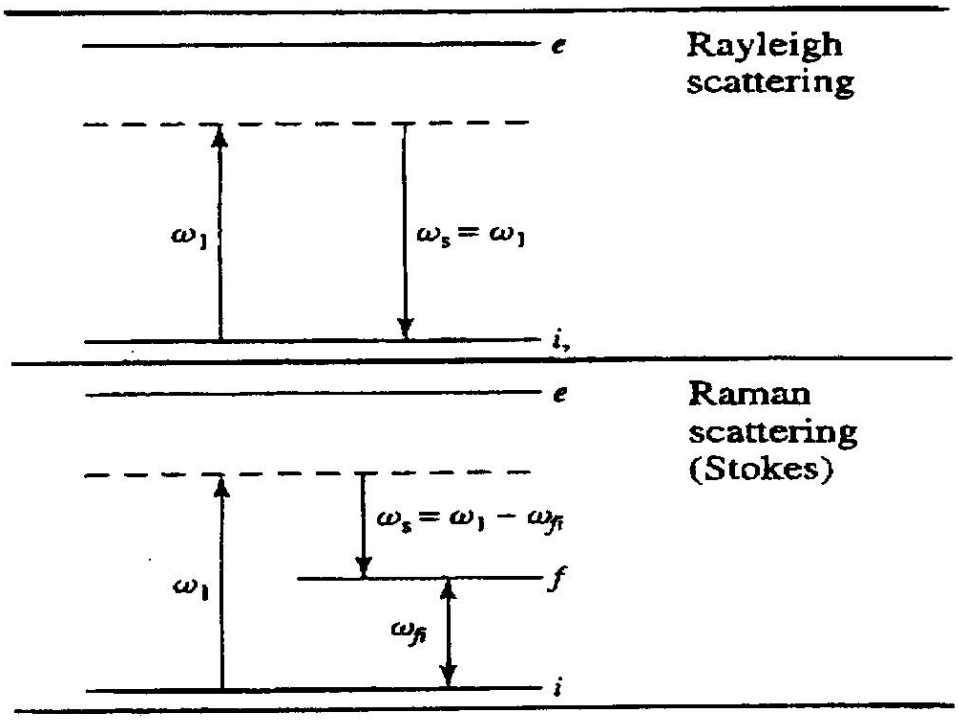


Fig 2.10 : Energy level diagrams for Rayleigh and Raman scattering.

The Raman Spectrum

A Raman spectrum is a plot of the intensity of the Raman scattered radiation as a function of its frequency difference from the incident radiation. The difference is called the Raman shift. Typically only the Stokes region is used.

Advantages and Disadvantages of Raman Spectroscopy

There are several advantages and numerous disadvantages of Raman Spectroscopy. One of the advantages is that no sophisticated sample preparation is necessary. It is a non-destructive (*in-situ* technique) that is relatively fast (spectrum acquisition time of 1 sec to several minutes). In addition there is relative lack of interference of adjacent peaks (aqueous solutions is not a problem) and characteristic spectra are used for the identification of compound/phases (fingerprint) and spartial resolution~1μm (micro-Raman).

The disadvantages are numerous among which are as follows; not all compounds are Raman active (need other complimentary technique such as IR spectroscopy to access all vibrational modes), it can only probe bulk properties of materials which are transparent to incident laser wavelength (otherwise a surface or near-surface technique is required), it develops inherent weakness of Raman effect (which can be overcome by intense sources (lasers) and efficient detectors (CCD) and it is fluorescent (which can be suppressed by using longer wavelength excitation).

2.3.2 The Classical theory of light scattering

An incident electric field ($\vec{E}_{inc}$) induces a dipole moment $\vec{P}$ in the material.

$$\vec{P} = \varepsilon_0 \chi(\omega) \vec{E}_{inc} \qquad (2.1)$$

where $\chi(\omega)$ is the susceptibility tensor (dipole moment per unit volume induced by a unit field) and $\alpha(\omega) = \varepsilon_0 \chi(\omega)$ is the polarizability (ability to be polarized). Therefore equation (2.1) becomes

$$\vec{P} = \alpha(\omega) E_{inc}$$

where the component P_i of the dipole moment, (i = x, y or z spatial directions is given by):

$$P_i = \sum_j \alpha_{ij} E_j$$

where α_{ij} is the polarizability tensor.

For a vibrating molecule: change in α_{ij}; Taylor expansion in normal coordinates:

$$\alpha_{ij}(\omega_{inc,}\xi) = \alpha_{ij}(\omega_{inc}) + \frac{\partial \alpha_{ij}}{\partial \xi} \xi e^{j(\bar{q}.\bar{r}l - \Omega_p t)} + ...$$

where ξ is the normal coordinate, ω_{inc} is the exciting frequency, $\bar{q}$ is the crystal momentum or wave vector of the mode and Ω_p is the frequency of the vibrational mode.

A molecule can vibrate in different ways, and each is referred to as a *vibrational mode*. Linear molecules have 3N−5 degrees of vibrational modes whereas nonlinear molecules have 3N – 6 degrees of vibrational modes (also called vibrational degrees of freedom). As an example H_2O, a non-linear molecule, will have 3 × 3 – 6 = 3 degrees of vibrational freedom, or modes.

Simple diatomic molecules have only one bond and only one vibrational band. If the molecule is symmetrical, e.g. N_2, the vibrational band will be observed in the Raman spectrum and will be absent in the IR spectrum. Asymmetrical diatomic molecules, e.g. CO, absorb in the IR spectrum. More complex molecules e.g. CH_2 has many bonds, and their vibrational spectra are correspondingly more complex, i.e. large molecules have many peaks in the IR spectra.

The induced polarization of an incident exciting wave $E_j = E_{0j} e^{j(\bar{k}_{inc}.\bar{r}l - \omega_{inc}t)}$ is given by

$$P_i = \sum_{j=x,y,z} \alpha_{0ij}(\omega_{inc}) E_{0j} e^{j(\bar{k}_{inc}.\bar{r}l - \omega_{inc}t)} + \sum_{j=x,y,z} \frac{\partial \alpha_{ij}}{\partial \xi} \xi E_{0j} e^{j[(\bar{k}_{inc}+\bar{q}).\bar{r}l - (\omega_{inc}+\Omega_p)t]} + ...$$

The term $\alpha_{0ij}(\omega_{inc}) E_{0j} e^{j(\bar{k}_{inc}.\bar{r}l - \omega_{inc}t)}$ indicates that the light induces a dipole moment which oscillates at the same frequency as the light, so that light of that frequency is re-radiated. This applies only for elastic or Rayleigh scattering. The term $\sum_{j=x,y,z} \frac{\partial \alpha_{ij}}{\partial \xi} \xi E_{0j} e^{j[(\bar{k}_{inc}+\bar{q}).\bar{r}l - (\omega_{inc}+\Omega_p)t]}$ indicates that the dipole moment is modulated by the light through the polarizability, itself modulated by molecular vibration (this is the inelastically scattered light). This is for Raman scattering (Raman-active mode). Conventionally, the scattering of light with a decrease in frequency is referred to as Stokes scattering whilst the converse is called anti-Stokes scattering.

CHAPTER 3

EXPERIMENTAL: SAMPLE PREPARATION AND CHARACTERISATION

The sample preparation procedure for this dissertation is similar to what others have reported which also used soild-state reaction method (Nagata et al., 2001), (Bouziane et al., 2005).

3.1 SYNTHESIS OF $SmFe_{1-x}Mn_xO_3$ SAMPLES

Polycrystalline samples of $SmFe_{1-x}Mn_xO_3$ ($0 \leq x \leq 1$) were prepared using a solid state reaction method. High purity oxides of Sm_2O_3 (99.999%), Mn_2O_3 (99.999%) and α-Fe_2O_3 (99.999%) were weighed on an ADAM AFP-210 L digital analytical balance, according to the stoichiometric ratio after calculations of the required masses. The weighed quantities were repeatedly and thoroughly ground to a powder in a pestle and mortar to ensure homogeneity.

The homogeneous powder was placed into a press tool similar to that shown in Fig 3.1. It was then pressed into a pellet of 6 mm in diameter by the application of a 4 kN force using a manually operated hydraulic press[2] (15 Tons) as shown in Fig 3.2, for 15 to 20 minutes. The resulting pellet was then heat treated in air, for 24 hours at 1200°C, and cooled at a rate of 5ºC per minute in a tube furnace.

[2] SPECAC Limited, UK

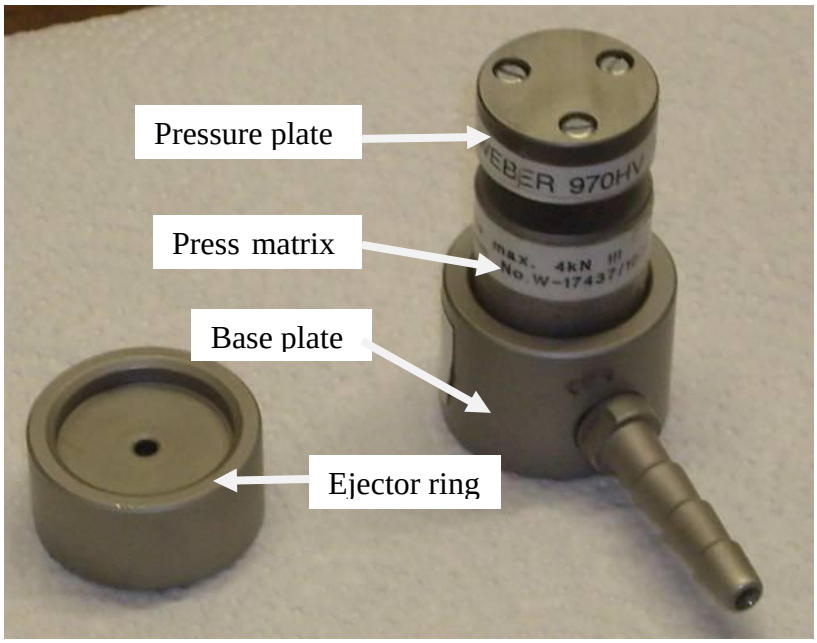


Fig 3.1 : Mini-pellet press tool.

Another sample with the same stoichiometric ratio for all the samples of $SmFe_{1-x}Mn_xO_3$ (x = 0, 0.2, 0.5, 0.8 and 1) was prepared and the resulting pellet was heat treated for 24 hours in air and quenched in liquid Nitrogen. The purpose of this was to ascertain whether there is still a contamination on the pellet. There is contamination arising from excess oxygen when heat treated in air. Quenching in liquid nitrogen on the other hand leads to segregation.

The heat treated pellet was then thoroughly ground in acetone (to prevent oxidation) in an agate pestle and mortar. It was again pressed into a pellet, and underwent a second heat treatment under similar conditions as before. This procedure was repeated for the preparation of all the stoichiometric compositions of $SmFe_{1-x}Mn_xO_3$ (x = 0, 0.2, 0.5, 0.8 and 1). All but one of the compositions was heat treated twice. The one exception was for the sample x = 0.8 which was heat treated three times during its preparation.

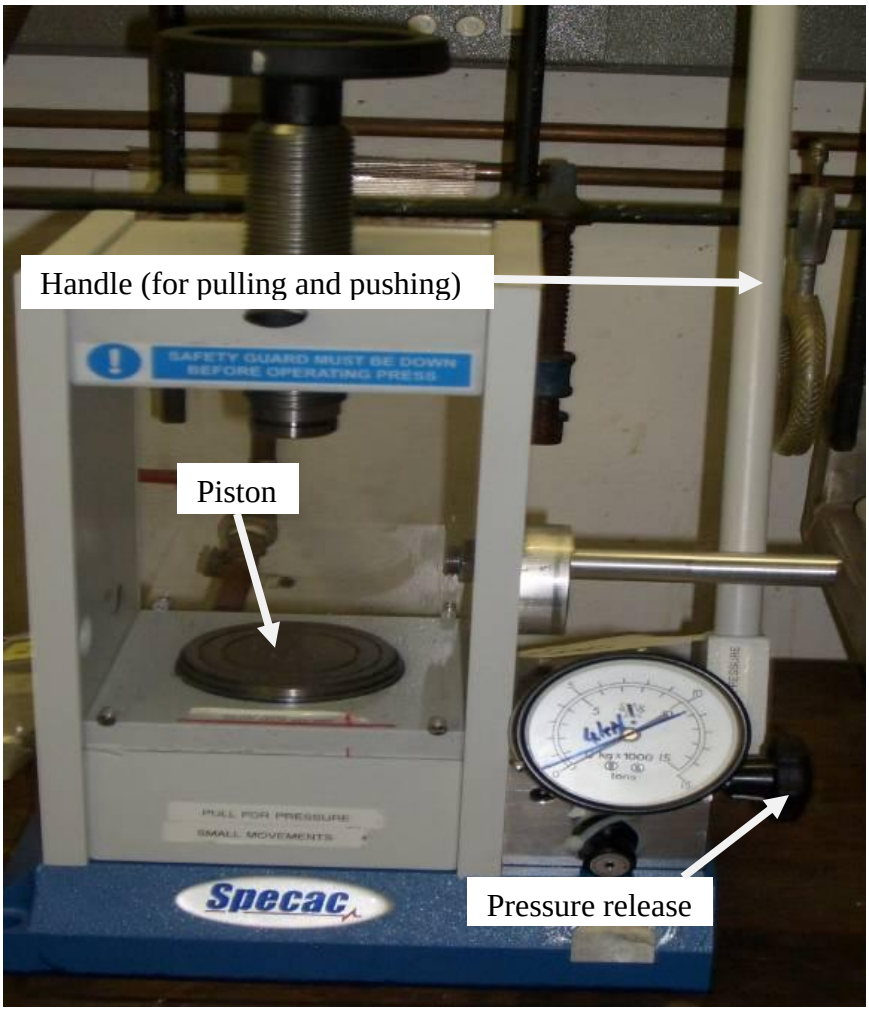


Fig 3.2 : Hydraulic press.

The second heat treated pellet was then ground repeatedly into a powder under acetone in a pestle and mortar as before (to prevent further oxidation). About 100 mg of the powder was then taken for ICP (Inductively Coupled Plasma) analysis in order to check for Fe/Mn ratio in the sample. If the ICP analysis agreed with the stoichiometric ratio of the Fe/Mn then an X-ray diffraction pattern and ^{57}Fe-spectroscopy spectrum was performed on the powdered sample. The synthesis process was repeated to check for reproducibility.

Pellets of 3 mm in diameter were also prepared using the special press tool in Fig 3.2 by applying a force of 4 kN. All the pellets prepared for all the compositions were synthesized by the same solid state reaction and the characterization techniques repeated as for the 6 mm pellets. The 3 mm pellets were prepared for magnetization measurements.

3.1.1 Procedure for Annealing

The furnace used for heating the pellets was EUROTHERM 2416 CG[3]. The furnace consist of the main ceramic tube at the centre of which are the heating elements. Another smaller tube (the central ceramic tube) which held the sample was placed into the main ceramic tube and glass wool was used to put it into place. The control panel was next to the main ceramic tube. This set up is shown in Fig 3.3.

The pellet was first placed inside a ceramic boat. The boat containing the pellet was then placed in the centre of the central ceramic tube which was then inserted into the main ceramic tube. Thereafter, the pellet was heat treated for 24 hours at 1200°C in air, following which it was cooled at a rate of 5ºC per minute in the furnace.

[3] Eurotherm 2416 CG from Carbolite, UK

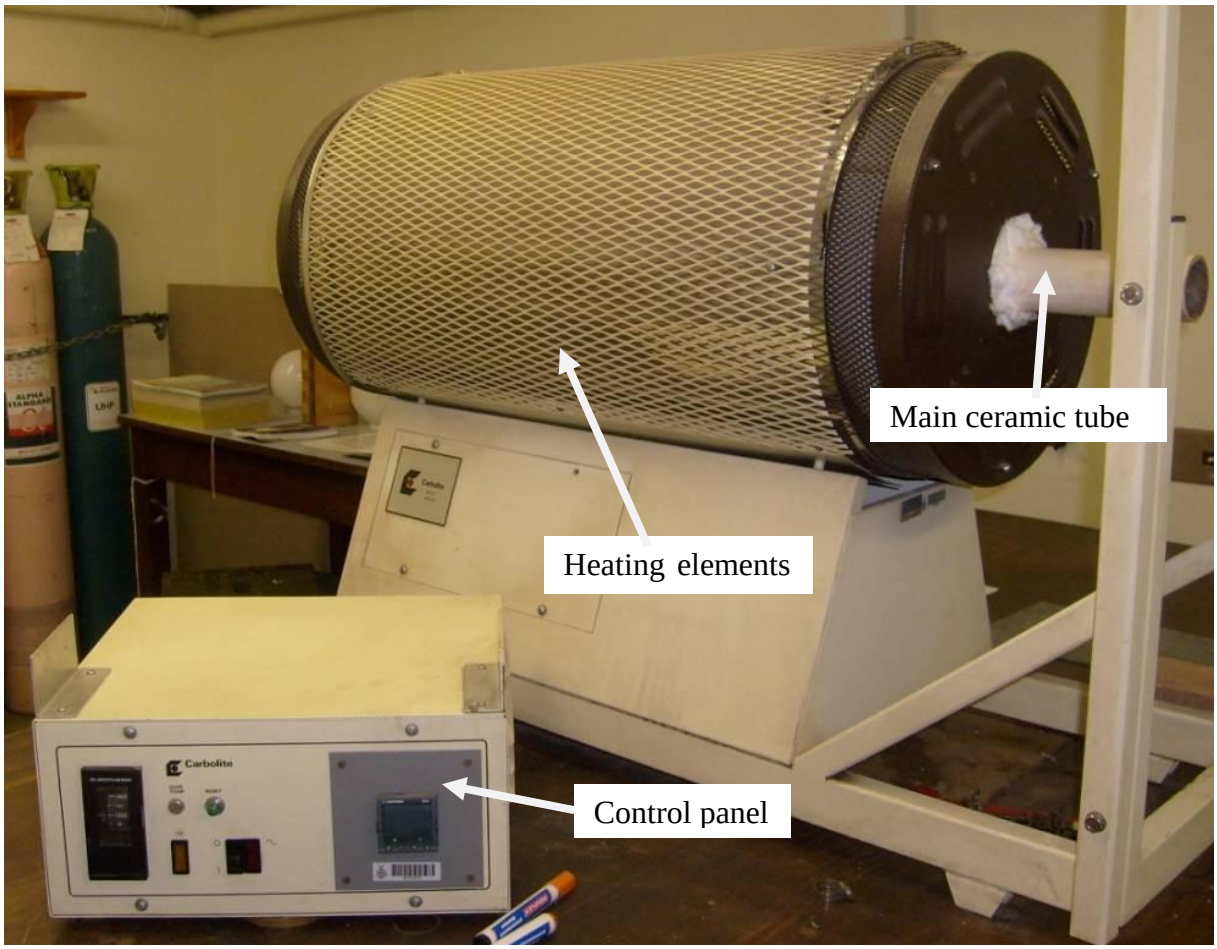


Fig 3.3 : EUROTHERM 2416 CG Carbolite furnace.

3.2 SAMPLE CHARACTERISATION

All the samples were characterised using X-ray powder Diffraction (XRD), ^{57}Fe spectroscopy, Micro-Raman spectroscopy and SQUID/MPMS measurements.

3.2.1 Procedure for X-ray Diffraction measurements

***Sample preparation, data collection strategy and analysis*:**

The prepared powder samples were placed into the circular cavity of a silicon single crystal wafer zero background sample holder as shown in Fig 3.4. A zero background sample holder is a single crystal cut on a direction such that it does not exhibit Bragg's diffraction.

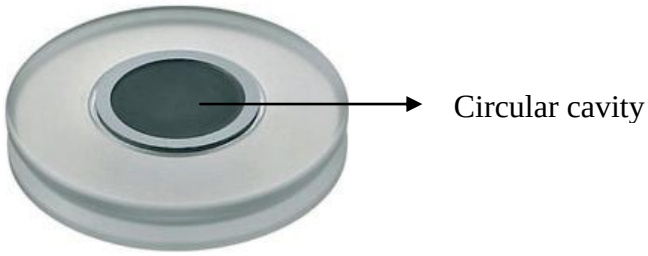


Fig 3.4 : Zero background sample holder.

The sample was evenly and randomly distributed on the sample holder using a glass slide. The sample holder with its contents was then inserted into the Bruker D8 Advance diffractometer[4] as shown in Fig 3.6, and the subsequent X-ray analysis was done. As for the pellet, it was abraded thoroughly (by scraping the surface with a scalpel) and cleaned with acetone before X-ray diffraction analysis was done. The sample was then glued down onto the centre of the sample holder with press-stick and XRD measurements taken. The acquisition times were in the order of 20 to 30 minutes for powder crystalline samples and 30 minutes to 1 hour for the pellets.

X-ray diffraction patterns were also obtained for powders and pellets in small quantities (~ 15 mg) and (~ 25 mg) respectively for $SmFeO_3$ and $SmMnO_3$.

[4] Bruker D8 Advance diffractometer from Bruker AXS GmbH, Germany

Brief description of the instrumentation

The schematic diagram of a diffractometer is shown in Fig 3.5.

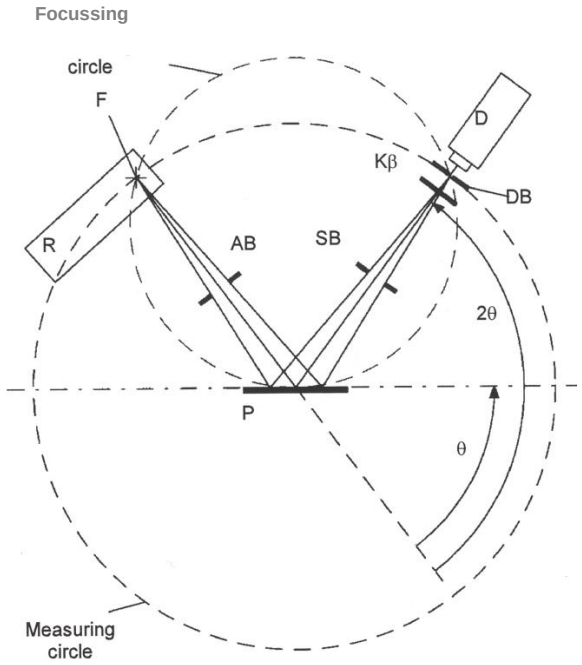


Fig 3.5 : Schematic diagram o f the beam path of Bruker D8 Advance diffractometer.

The symbols indicated in Fig 3.5 are defined as:

θ = incident angle, 2θ = Diffraction angle, AB = Aperture slit, D = Detector,
DB = Detector slit, F = Focus, Kβ = Kb filter, P = Sample,
R = X-ray tube, SB = Scattered-radiation slit.

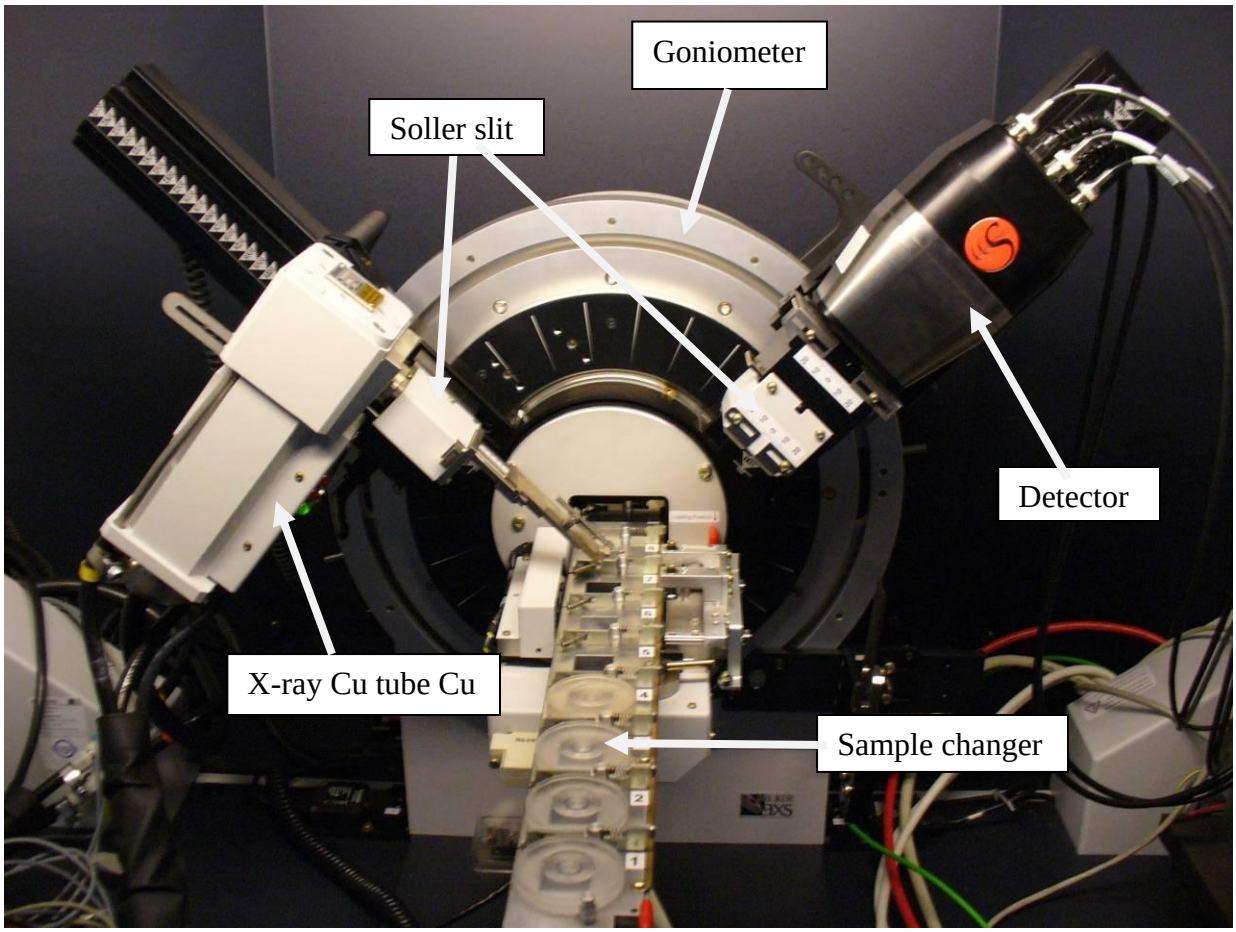


Fig 3.6 : View of the Bruker D8 Advance Diffractometer.

Details of Bruker D8 Advance Diffractometer

Instrument parameters :

The instrument was equipped with a copper X-ray generator tube ($CuK\alpha_1$ & $CuK\alpha_2$ radiation: λ = 1.5418 Å; 40 kV, 40 mA), and a VÅNTEC high resolution detector. Bragg Brentano geometry with a divergence slit of 0.6 mm and 0.8 mm receiving slit (detector slit) were used. The diffraction patterns were collected by steps of 0.014° (2θ) over the angular range 10° to 90°, with a counting time of 0.5 s per step. To

further improve the signal to noise ratio, where necessary and to reduce the effects of atomic fluorescence, detector limits were readjusted to accept a smaller range of incoming energy.

The Bruker Diffrac Plus Evaluation software was used to establish the precise positions of the peaks using structure models obtained from the powder data file database. Rietveld refinements were done using TOPAS Version 3 (Coelho, 2003) using a fundamental parameters approach. Structure models, with which the Rietveld refinements were carried out, were obtained from the Inorganic Crystal Structure Database (ICSD), Version 1.4.6 Release 2 (2009).

3.2.2 Procedure for Mössbauer Spectroscopy measurements

The pellets were cooled down to room temperature after each heat treatment before being ground in acetone. From the resulting powder 35 mg was weighed and mixed with cremora milk powder (dilutant) to achieve a uniform loading across the absorber holder. The mixture was then placed in a copper powder-clamp sample holder, 1.5 cm in diameter. The sample in the form of powder is spread uniformly and sandwiched between the two mylar windows and clamped. There should be no gap or pin-holes. The ^{57}Fe spectra were acquired using 35 mg of the samples measured at room temperature and 45 mg of the sample was used for low temperature (90 K) measurements. A ^{57}Co in Rh matrix source of strength ~20 mCi was used in the Mössbauer measurements. The velocity scale was calibrated by means of an Fe foil of 12 μm thickness (≈ 10 mg/cm^2 of Fe), with Normos-90 software[5] used for the analysis.

During the acquisition of the Mössbauer spectra 35 – 45 mg of material was used amounting to thickness of 20.6 – 26.5 mg/cm^2 of material. For a single line 5 mg/cm^2

[5] Normos-90 software from Wissel Instruments, Germany

of Fe is required. For a doublet, resonance is distributed between the two lines which means 10 mg/cm^2 of Fe may be used and for sextet it requires 30 mg/cm^2 of Fe. This quantity of material was used because the count rate and resonance effect (intensity) are functions of the absorber thickness in a spectrum. For a reliable analysis of spectra, determination of the thickness of the absorber is very important. If the absorber is too thick there will be too much electronic absorption, and also extrinsic broadening of the linewidths (Long et al., 1983). The size of the absorbers is inversely proportional to the iron concentration in the sample. Choosing an appropriate optimum thickness for the sample is vital where the iron concentration is low (Murad and Cashion, 2004). In this case there is a high proportion of heavy elements or the M_{fe}-value is small (M_{fe} being the mass fraction of the heavy element). Most of the absorption is from the Samarium element therefore appropriate thickness of the absorber becomes necessary. The mass absorption coefficients are given as a function of wavelength on X-rays and have been tabulated at 14.4 keV for all elements by (Long et al., 1983).

Instrumentation **:** *Mössbauer equipment*

The Mössbauer equipment basically consists of a source (^{57}Co) in a rhodium matrix as a source of gamma rays (γ-rays), a drive mechanism for producing a Doppler velocity and a Kr-CO_2 detector which recorded the transmitted gamma rays. The spectra were obtained with a constant acceleration and were collected over 1024 channels. A commercial Personal Computer Analyzer (PCA) controller card was used for waveform generation, energy discrimination and multi-channel scaling. The discriminator allows for the selection of 14.4 keV peak. The dwell time is 100 μs per channel. The set up is shown in Fig 3.7.

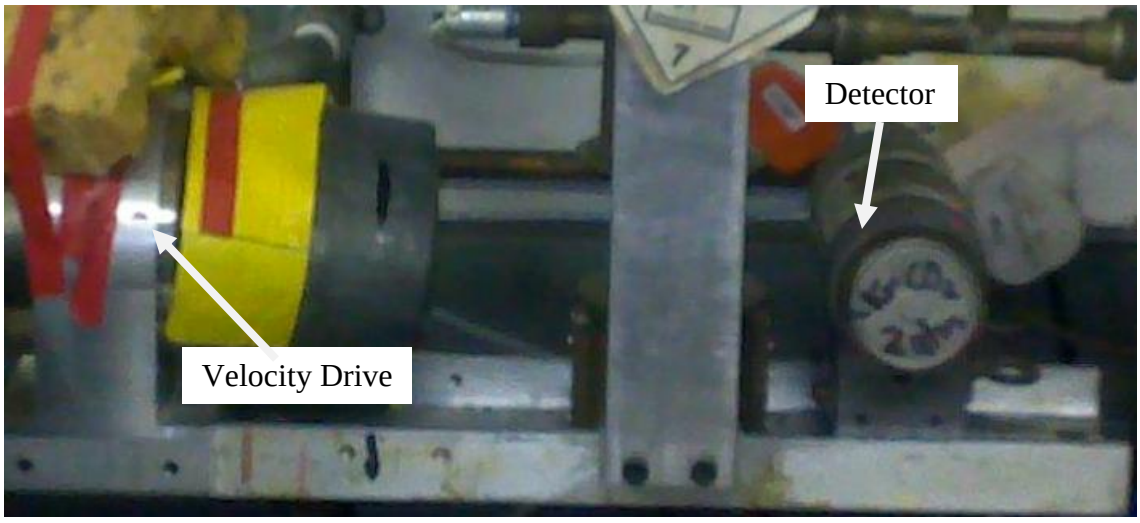


Fig 3.7 : Mössbauer Spectrometer set-up.

The Mössbauerspectrum is a record of the transmission rate of the resonant γ-rate, as a function of Doppler velocity between the source and the absorber. By mounting the source on a mechanical *constant-velocity* drive the total number of counts can be registered in a *fixed time*, at constant velocity, and subsequently re-measured at different velocities. The *multi-channel analyzer* (MCA) employed as data-storage, is *synchronized with vibrator sweeps*. A square wave from the multi-channel analyzer with leading edges at channels 1024 is integrated to give a systematic triangular signal.

Low-temperature facility for Mössbauer spectroscopy

The low-temperature facility for Mössbauer consists of a cryogenic part and a vibrational assembly. The liquid nitrogen (LN2), Cold finger Cryostat lower portion is made of copper and the upper part is made of a thin-walled stainless steel (SS) neck, linked to main Dewar. The lower part contains a loading sample chamber and a sample mount. The sample chamber is made of copper so as to maintain uniformity of the temperature in the region where the sample is kept and to attain the lowest

temperature that is possible. The thin-walled SS tube supports the large temperature gradient between the copper portion and the top portion which is at room temperature. A schematic diagram of the cryogenic part is shown in Fig 3.8 showing the sample holder and other cryogenic parts. The sample in the form of powder was prepared for low temperature measurement (the preparation of the powder was the same as the one done for room temperature measurement). The sample holder was carefully mounted on the sample mount area of the cryostat copper cold finger with press-stick. No excessive force should be used when inserting or removing the sample. After that the sample chamber was placed into position and closed with the O-ring clamp which provides vacuum sealing. It was then evacuated with a single-stage pump.

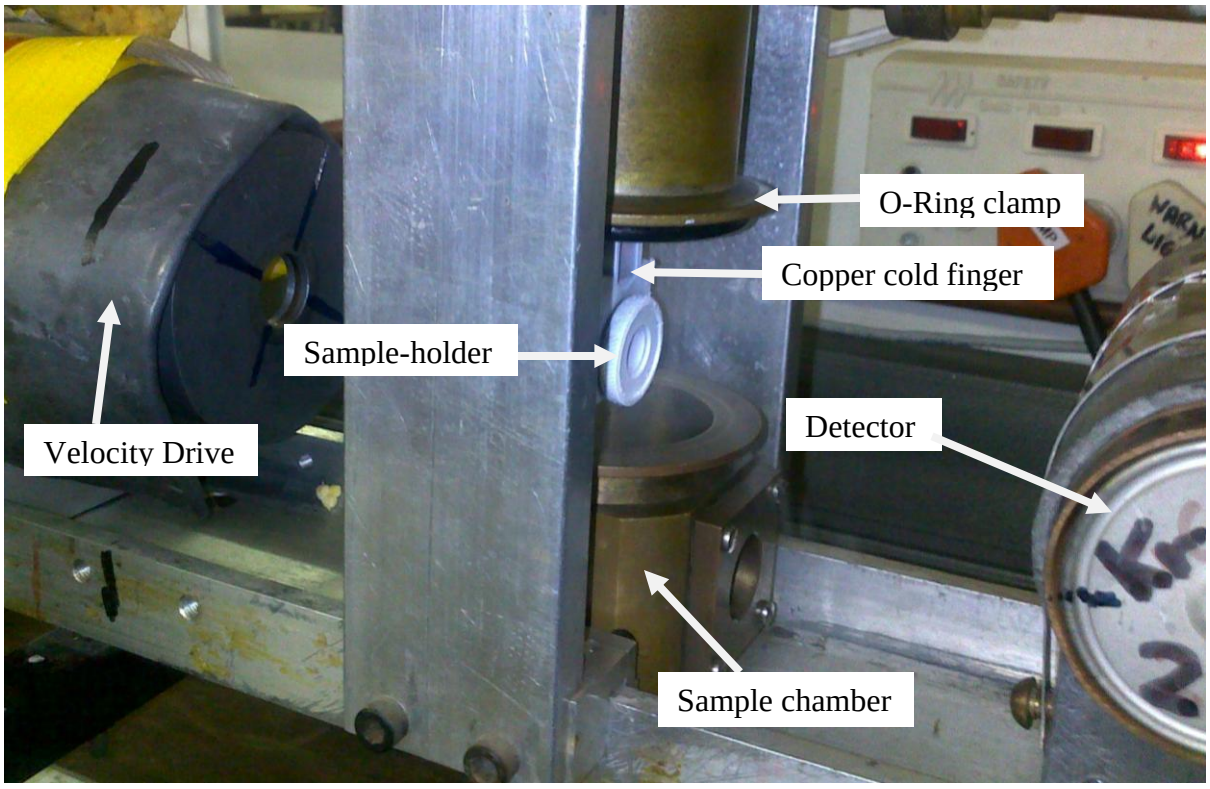


Fig 3.8 : Cold finger cryostat for low-temperature measurements.

A ^{57}Co in Rh matrix Mössbauer source of strength ~20 mCi was also used here to acquire the Mössbauer spectra. A standard 12 μm thickness iron foil was used to record the absorption spectra for calibration. Below is the calibration detail. The absorber is mounted in the sample holder in the low-temperature facility to record the spectra at 297 K.

```
Job file: fe2o3c.job
Spectrum: fe2o3c.mos
Plt file: fe2o3c.plt

Values of the fit-variables
Index Name      Initial                Final                  Error (1*STD)
  1 BKG(1)       762260.                763185.      +-         70.9594
 15 WID         0.250000               0.273064     +-       0.992083E-03
 16 ARE         0.500000               0.467605     +-       0.138805E-02
 17 ISO         0.370000               0.263863     +-       0.353869E-03
 18 QUA        -0.200000              -0.217475     +-       0.716597E-03
 19 BHF          51.7000                51.7208     +-       0.273320E-02
 26 A13          1.79500                2.55733     +-       0.139248E-01
 27 A23          1.71000                1.81740     +-       0.104784E-01
Final results for the Chi-2 fitting parameter
Chi-square (normalized)                =     5.66
Observed deviation                     =     51.8     std. deviations
95% confidence interval (2*std. dev.) = 1 +-     0.180
          Table of final areas and quality factors
Sub.  Lines  Area         Error  Area (%)  Error (%) ET-total QT-total
  1      6   0.467605   0.001388 100.000   0.297    1.090    374.737
Total spectrum
Area                                   =   0.467605 +-   0.001388
                  End of calculations
```

RAMAN INSTRUMENTATION

The schematic diagram of the Raman set-up (depicted in Fig 3.9) below shows the various optical components of the spectrometer used in our experiment.

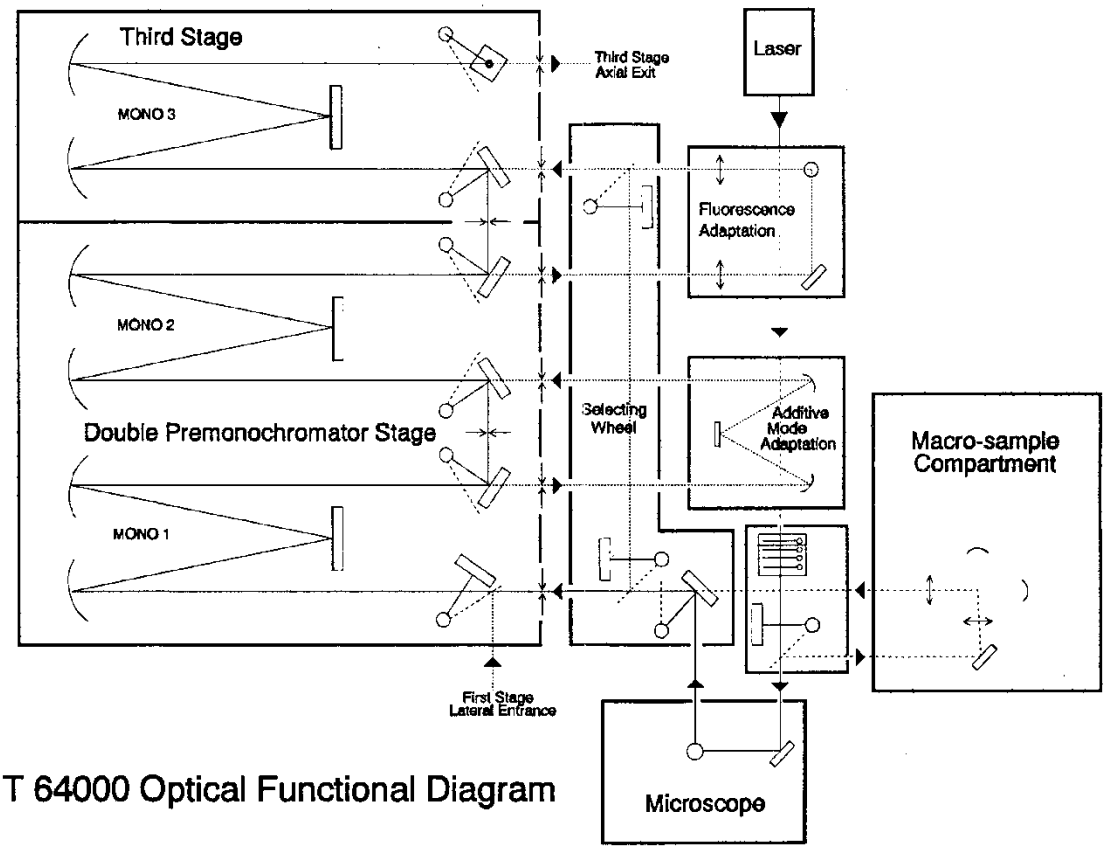


Fig 3.9 : Schematic diagram of the Raman Spectrometer.

3.2.3 Procedure for Raman Spectroscopy measurements

Room temperature Raman measurements

The Raman spectra were obtained at room temperature with a Jobin-Yvon T 64000 Raman spectrometer with CCD detector. A small quantity of the powdered sample was placed onto a microscope slide. The slide was then placed on the stage of an Olympus BX – 40 microscope of the Jobin-Yvon T 64000 micro-Raman facility. The Raman spectrometer setup is shown in Fig 3.10. The laser beam was focused onto the surface and viewed via CCD camera and monitor.

In the setup a 50x objective was used to focus the laser beam on the sample surface and to collect the scattered light. The 514.5 nm of Ar^+ laser was used for excitation. A low laser power of ~200 μW at the sample was used to minimize possible localized heating. Data acquisition times of 120 to 180 seconds were thus necessary.

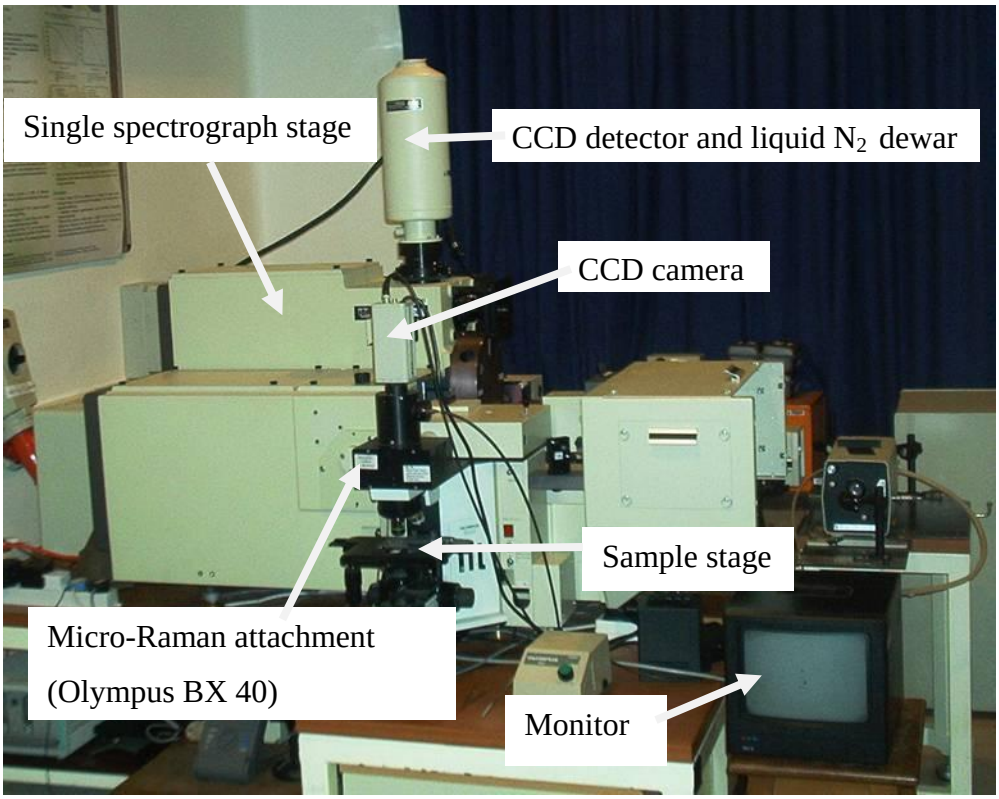


Fig 3.10 : Raman Spectrometer set-up for room temperature measurements.

Low-temperature Raman measurements

An Oxford Instruments Microstat^{He} continuous flow liquid helium microscope cryostat (shown in Fig 3.11) was used for low temperature Raman experiments. The cryostat was used in conjunction with an Oxford Instruments GFS 300 liquid cryogen transfer tube, a GF3 diaphragm vacuum pump (for cryogen flow), a VC41 gas flow controller, an Oxford Instruments ITC4 temperature controller and a Pfeiffer turbo-molecular pump with rotary backing pump for vacuum pumping duties. The vacuum was measured via a combined Pirani / cold cathode gauge. The temperature sensor of the cryostat was a RhFe thermocouple. Liquid nitrogen was used as the cryogen for measurements at 77 K. A stability of ±0.2 K is quoted in the manual for liquid nitrogen.

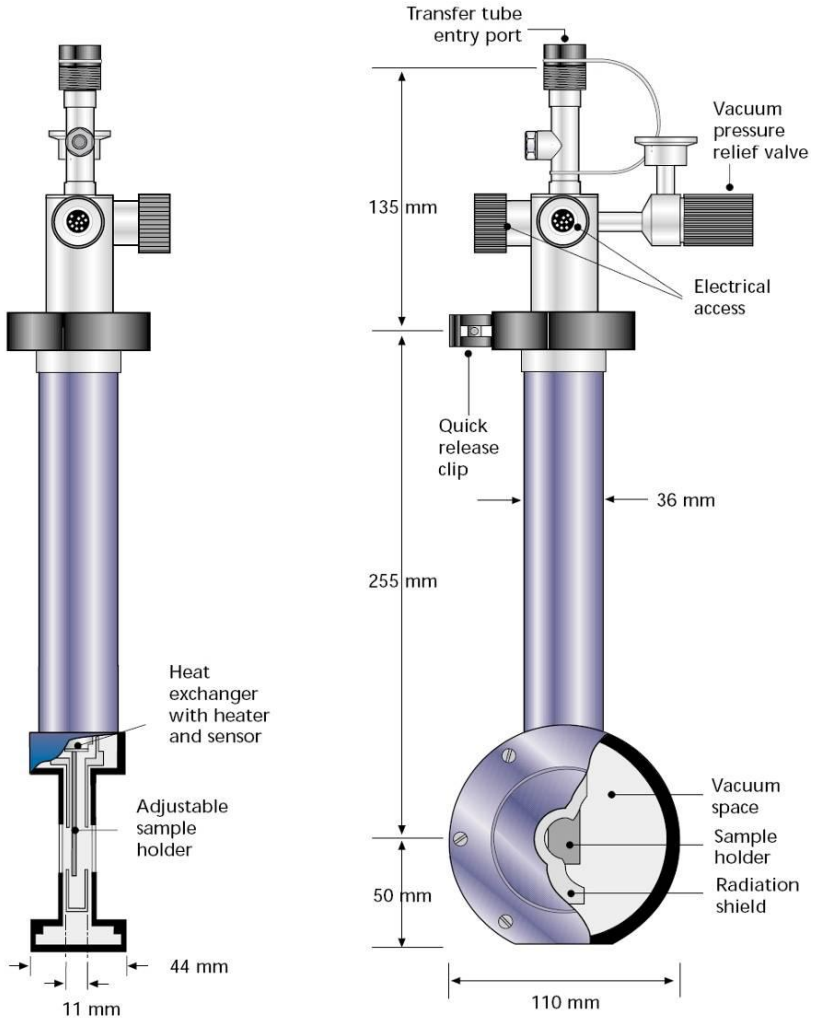


Fig 3.11 : Diagrammatic representation of the Oxford Instrument Microstat^{He} microscope cryostat used for some of the low temperature measurements.

In the cryostat, the samples were mounted in vacuum on a cold finger attached to a copper heat exchanger block. The mounting was facilitated with Apiezon "L" vacuum grease to keep the pelleted samples in position and ensure good thermal contact with the cold finger. Optical access to the samples was via Spectrosil B windows. A vacuum of $< 5\times10^{-5}$ Torr was sufficient for trouble-free low temperature operation. The cryostat was clamped to the motorised X-Y stage of the Olympus

microscope via a custom-built attachment, allowing for measurement of several small samples at low temperature.

3.2.4 Magnetization measurements

For magnetization measurements the pellets of 3 mm diameter were used. The pellets were shaped into cubes of 1 mm × 1 mm × 1 mm by abrading. The cubes are then cleaned with acetone and inserted in a folded piece of straw that is used as a sample holder. The magnetization measurements were performed with a DC SQUID (Superconducting Quantum Interference Device) magnetometer Quantum Design MPMSXL (Magnetic Properties Measurement System) in the temperature range between 2 K and 400 K.

Details of the SQUID Magnetometer;

A SQUID Magnetometer of the type Quantum Design MPMSXL is a helium cryostat with a superconducting magnet. The helium gas controls the sample temperature. The SQUID detector (which is a Josephson contact loop) is at the core of the apparatus and the measured quantity is the electronic magnetic dipole moment μ of the sample with respect to the direction parallel the applied magnetic field.

In order to investigate the magnetic properties of a sample, it is exposed to the field of a superconducting magnet and gradually moved through a pick-up coil system. The pick-up coil system is essentially an arrangement of induction coils. The coils are wound in a configuration in which the upper and lower single turns are counter wound with respect to the two-turn centre coil. This is so as to reject interference from nearby magnetic sources. A magnetized sample induces a voltage at each step while passing the coil arrangement stepwise. The SQUID detector measures the induced voltage. The sensor is a superconducting ring which has weak-links. At these

positions the critical current is significantly reduced. The magnitude of the DC current, which is proportional to the number of magnetic flux quanta is a measure of the change of the magnetic flux density caused by the magnetization of the sample as it moved through the pick-up coil system. The voltage can be plotted as a function of the sample position if the SQUID voltage is read at a large number of points. A set of such data is called the SQUID response. The SQUID response is fitted using the MPMSXL software to yield the sample magnetization. A schematic diagram of a MPMSR is shown in Fig 3.12.

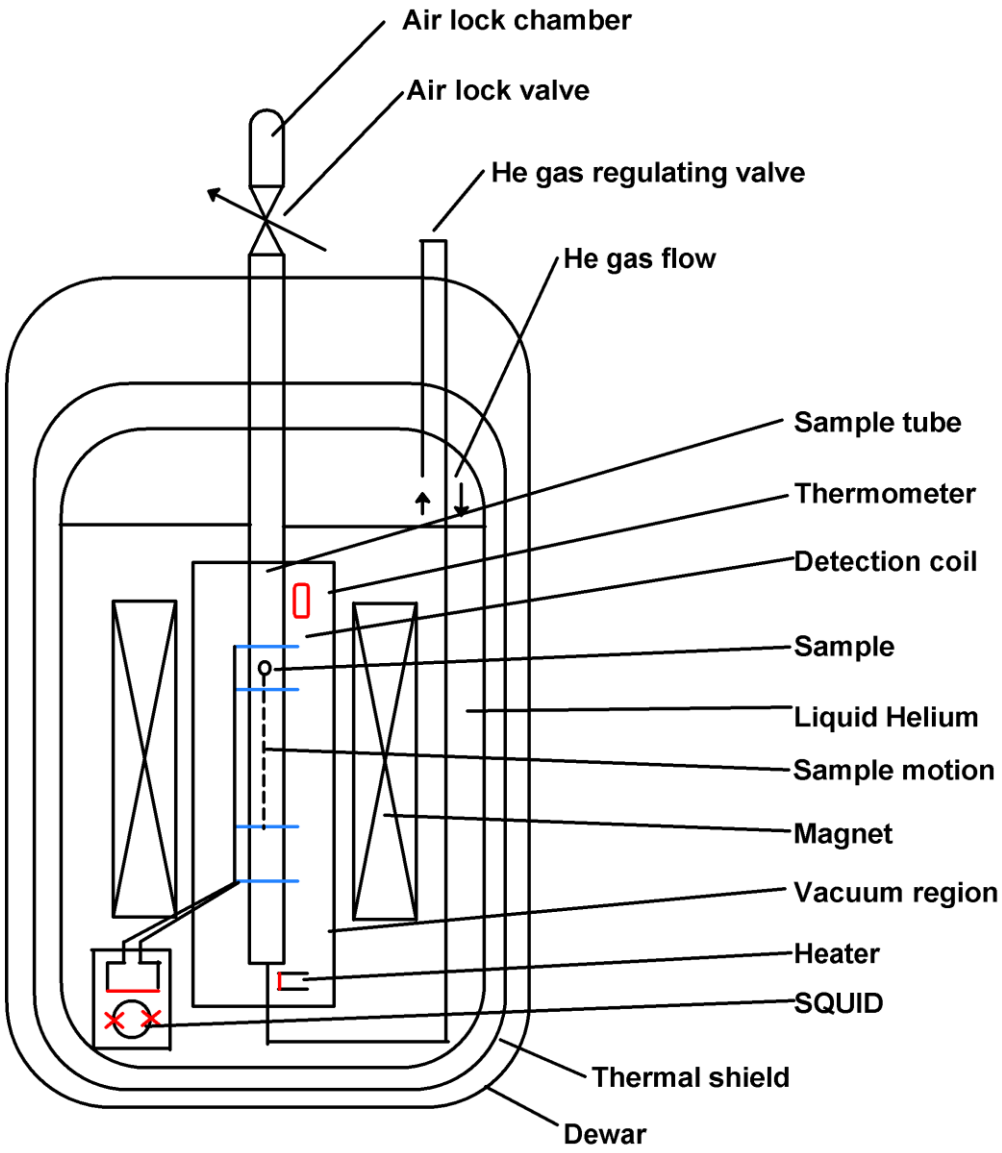


Fig 3.12 : Schematic diagram of a MPMSR. Adapted from L. Fagaly, *Review of Scientific Instruments*, 2006, 101101.

Procedure for magnetization measurements

The sample was inserted in a folded piece of straw that is used as a sample holder. The sample holder and its content are then inserted into Fiber optic of about 2 m in length. The sample is exposed to the field of a superconducting magnet and gradually

moved through the pick-up coil system (this is essentially induction coils). The sample is magnetized by a constant magnetic field and the magnetic moment of the sample is measured, producing a DC magnetization curve *M(H)*.

CHAPTER 4

EXPERIMENTAL RESULTS AND ANALYSIS

This chapter gives a detailed description of the experimental results obtained in this study. The results are divided into four parts namely X-ray diffraction (XRD), Mössbauer spectroscopy, Raman spectroscopy and magnetization measurements.

4.1 XRD CRYSTALLOGRAHICAL PROPERTIES

The powder X-ray diffraction (XRD) patterns of all the samples have shown that the compound is single phase. The XRD patterns of the sample were refined by the Rietveld method (Rietveld, 1969). From the refinements, the crystal structure of all the samples of $SmFe_{1-x}Mn_xO_3$ (x = 0, 0.2, 0.5, 0.8 and 1) was determined to be an orthorhombic structure of the space group *Pbnm*. The crystal structure of orthorhombic $NdFeO_3$ with space group *Pbnm* is shown in Fig 4.1 (Singh et al., 2008).

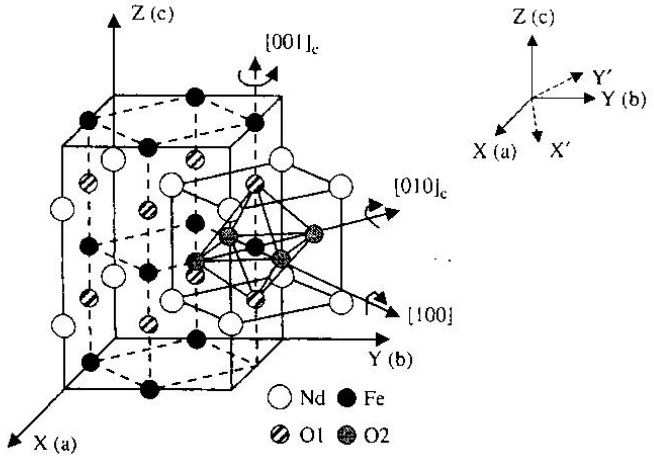


Fig 4.1 : Crystal structure of orthorhombic of $NdFeO_3$.

All the samples with an average volume of 232.4 $Å^3$ obtained are black crystallized powders except for $SmFeO_3$ ($x = 0$) which is dark brown. The clearly visible peaks of the spectra of Fig 4.2 show that the XRD patterns have well-defined reflections. All the samples were measured under the same conditions. The XRD patterns of $SmFeO_3$ ($x = 0$) shown in Fig 4.3a and $SmMnO_3$ ($x = 1$) in Fig 4.4a are in agreement with those reported in the Inorganic Crystal Structure Database (ICSD#=27276) and (ICSD#=95491) in Figs 4.3b and 4.4b, respectively. There are no XRD patterns for $x = 0.2$, 0.5 and 0.8 from the database. The lattice parameters *a*, *b* and *c* of $SmFeO_3$ and $SmMnO_3$ are also in agreement with those reported in the literature [(Treves, 1965), (Wang et al., 2005)] (see Table 1). The experimental resolution for all the XRD spectra was measured with respect to the peak-shift measurements. Counting time was chosen in order to obtain, for each peak position a statistical error of $2\theta \pm 0.01°$ for a confidence level of 99.7% (Convert and Miege, 1992).

The XRD patterns of all samples are shown in Fig 4.2. The lattice parameters *a*, *b*, *c*, volume and the strain parameter $s = 2(b - a)/(a + b)$ (Alonso et al., 2000) obtained for all the samples are shown in Table 1. Fig 4.5 shows the relationship between the lattice constants and the Mn content x. The lattice constants *a*, *b* and *c* determined from the refinement are shown in Fig 4.5 as a function of the Mn content. The lattice parameters *a* and $c/\sqrt{2}$ decreases with increasing Mn content *x* while the lattice parameter *b* increases with the Mn content *x*. When $x < 0.65$, the lattice parameter $c/\sqrt{2}$ is greater than the lattice parameter *a* and when $x > 0.65$, the lattice parameter *a* becomes larger than $c/\sqrt{2}$. This is as a result of the two distortions namely the cooperative tilt of the MnO_6 octahedra (the O-type with $a < c/\sqrt{2} < b$) and that related to the Jahn-Teller effect (the O′-type with $c/\sqrt{2} < a < b$) are present in the sample similar to that of $EuFe_{1-x}Mn_xO_3$ ($x = 0.0 – 1.0$) reported by (Li et al., 1998). The Jahn-Teller (J-T) distortion of the trivalent Mn in the octahedral sites is due to its $3d^4$

electron configuration (Li et al., 1998). This distortion does not change the lattice symmetry (*Pbnm*) but modifies the cell deformation from the O-type to O′-type.

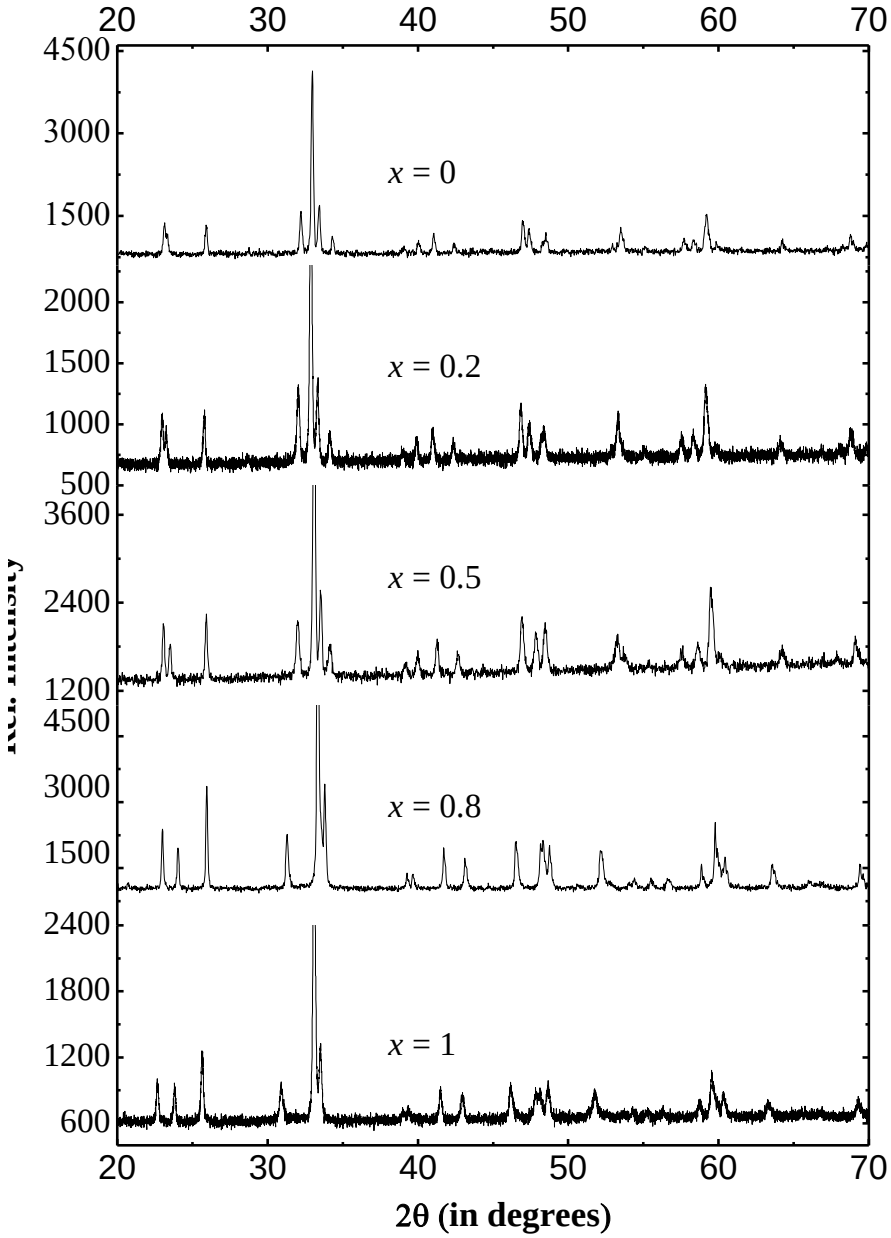
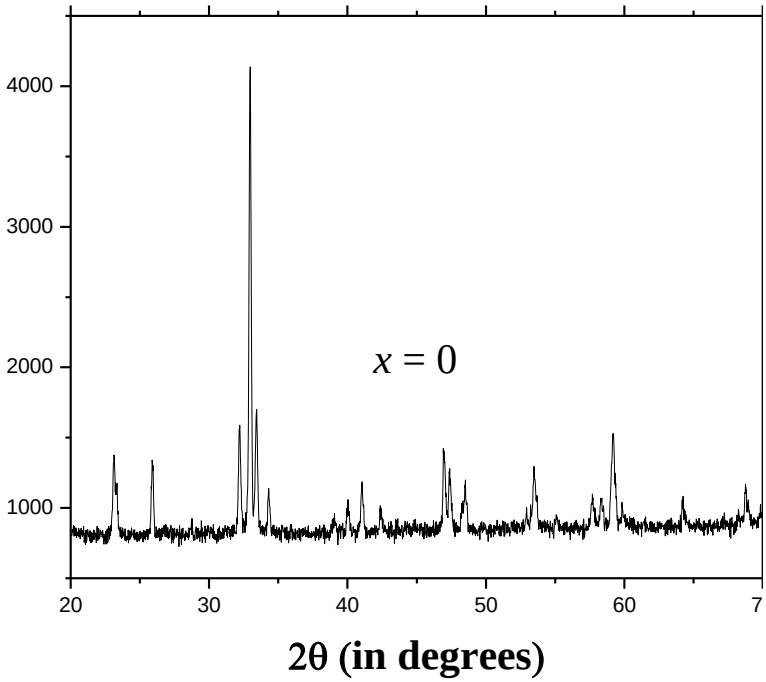


Fig 4.2 : XRD spectra of $SmFe_{1-x}Mn_xO_3$ (x = 0, 0.2, 0.5, 0.8 and 1). All the samples were measured under the same conditions.



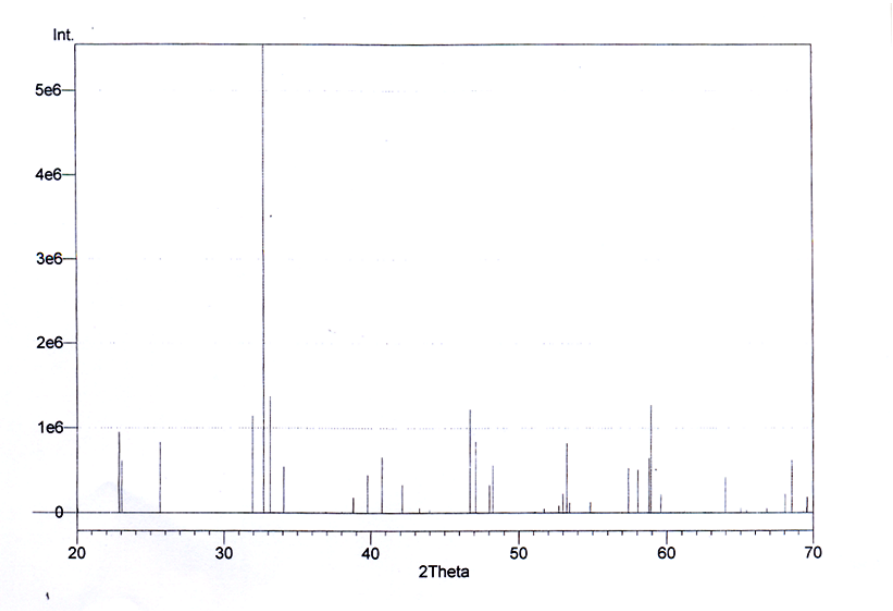
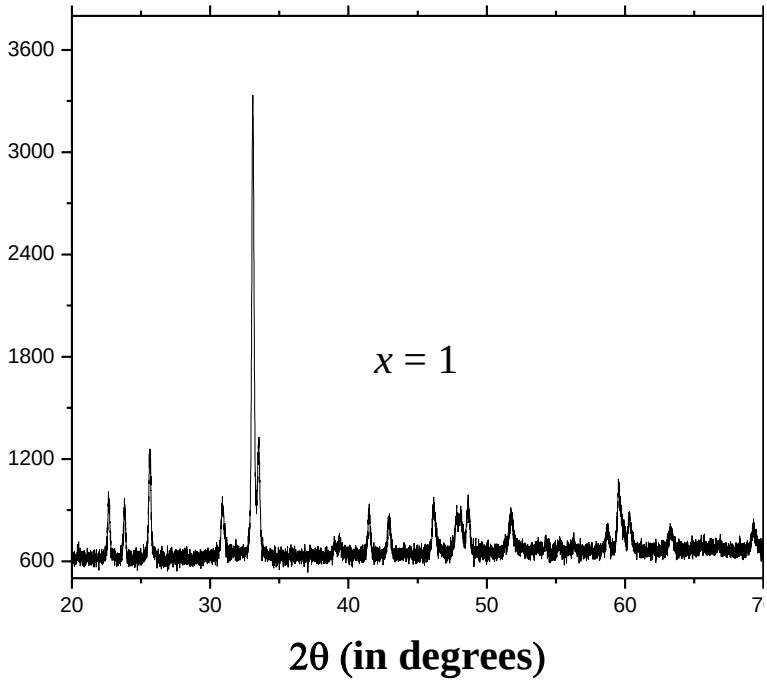


Fig 4.3a : XRD pattern of $SmFeO_3$ (x = 0) obtained from experiment and Fig 4.3b : XRD pattern of $SmFeO_3$ (x = 0) from the database (ICSD#=27276).



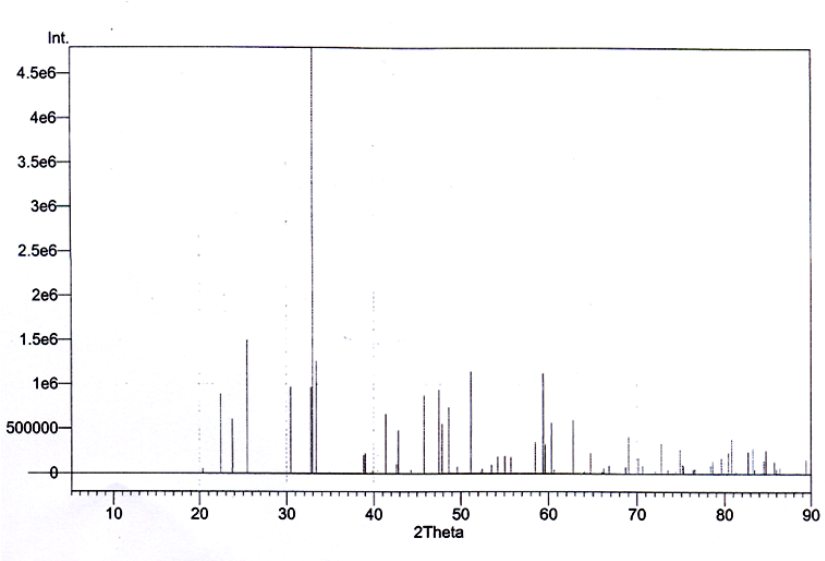


Fig 4.4a : XRD pattern of $SmMnO_3$ obtained from experiment and Fig 4.4b : XRD pattern of $SmMnO_3$ from the database (ICSD#=95491).

Table 1 : Lattice parameters of $SmFe_{1-x}Mn_xO_3$ (x = 0, 0.2, 0.5, 0.8 and 1).

Sample	a (Å)	b (Å)	c (Å)	Volume (Å^3)	S
♣$SmFeO_3$	5.394	5.592	7.711	232.6	-
♣♣$SmFeO_3$	5.400	5.597	7.711	232.6	-
x = 0	5.401	5.601	7.711	233.3	0.036
x = 0.2	5.394	5.607	7.687	232.5	0.039
x = 0.5	5.380	5.633	7.638	231.5	0.046
x = 0.8	5.366	5.697	7.564	231.2	0.060
x = 1	5.363	5.806	7.497	233.4	0.079
∗$SmMnO_3$	5.390	5.710	7.680	236.0	-
∗∗$SmMnO_3$	5.358	5.825	7.483	232.5	-

♣$SmFeO_3$ (Treves, 1965), ♣♣ $SmFeO_3$ (Marezio et al., 1970), ∗$SmMnO_3$ (Ciambelli, 2000) and ∗∗$SmMnO_3$ (Wang et al., 2005)

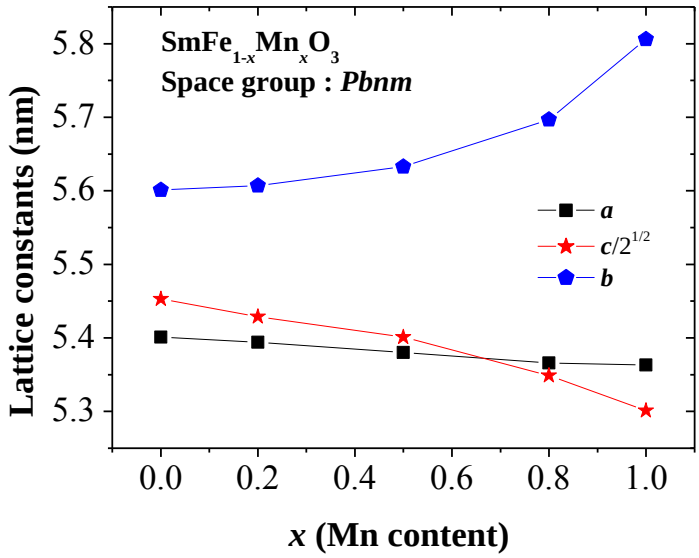


Fig 4.5 : Mn content dependence of the refined orthorhombic lattice constants *a*, *b* and *c*/√2. The solid lines indicate trends of the experimental data.

It can be seen from Table 1 that the lattice constants *a* and *c* decrease as the Mn content increases while the lattice constant *b* increases with the Mn content in the sample. This is due to the tilting of MnO_6 octahedra in *Pbnm* perovskites (Alonso et al., 2000). The constant *a* equals $c/\sqrt{2}$ at $x \approx 0.65$. This is where the effect of the Mn^{3+} ions become more dominant and the J-T distortion (the O'-type) takes over as shown in Fig 4.5. The orthorhombic strain *s* increases throughout the series as the Mn content increases in the specimen. The increase is twofold, firstly, because of octahedral tilting and secondly as a measure of the local distortion of the octahedron (i.e. J-T effect). Both effects influence the lattice parameters (Alonso et al., 2000).

4.2 MÖSSBAUER SPECTROSCOPY

The experimental Mössbauer spectra recorded at room temperature (RT) (293 K) for $x = 0$, 0.2, 0.5 and 0.8 are shown in Fig 4.6 and those at low temperature (90 K) for $x = 0.2$, 0.5 and 0.8 are depicted in Fig 4.7. All the spectra are fitted using the NORMOS-90[6] program. The hyperfine interaction parameters are given in Table 2.

The parameters obtained for the room and low temperature measurements are shown in Tables 2 and 3 respectively. The symbol *x* denotes the Mn content, δ denotes isomer shift (relative to Fe metal), QS denotes quadrupole splitting, Bhf denotes magnetic hyperfine field, Γ denotes line width, E.A. denotes Experimental abundance, T.A. denotes theoretical abundance and *n*(Fe) denotes the number of iron ions in the nearest neighbor octahedral site.

The Mössbauer spectrum of $SmFeO_3$ at room temperature exhibit a well resolved sextet with parameters shown in Table 2, very close to those reported in literature (Bashkirov et al., 2005). The spectrum for $x = 0$ was fitted with one sextet. The spectrum for $x = 0.2$ was fitted with four magnetic sub-spectra. The Mössbauer

[6] Normos-90 program from Wissel Instruments, Germany.

spectrum of x = 0.2 shows that the hyperfine field at ^{57}Fe nuclei has a distribution of values, depending on the number n of Mn^{3+} ions on the six nearest neighbor sites of Fe^{3+} ions (Li et al., 1998), (Nishihara, 1975) .

The probability of Fe^{3+} with n neighboring Mn^{3+} ions can be calculated as a function of x (where x is the ratio of Mn^{3+} ions to the sum of Mn^{3+} and Fe^{3+} ions in the sample) from the binomial distribution of the compounds of $RFe_{1-x}Mn_xO_3$ (Gibb, 1983b)

$$P(n) = \frac{6!(1-x)^n x^{6-n}}{(6-n)!n!}$$

It was found that the components (An, n = 1, 2, 3 or 4) of each spectrum are assigned to Fe sites having 6–n Fe and n Mn neighbours. This behavior has already been found in many related ferrite compounds (Gibb, 1983b), (Gibb, 1983a), (Li et al., 1998), (Nishihara, 1975).

The spectra of x = 0.2 at room temperature (RT) and x = 0.2 and 0.5 at low temperature (LT) were fitted with four sextets each, indicating the distribution of Mn ions around Fe ions in the sample. The spectrum for x = 0.5 at RT was fitted with one doublet and a sextet with a small magnetic hyperfine field (Bhf) indicating a collapsed magnetic field (from electronic relaxation effects). The spectrum for x = 0.8 was fitted with a single doublet at RT and LT. There was no spectra for x = 1 because it contains no Fe in the sample. The experimental resolution for all the spectra is about 0.02 mm/s and the error of the fitting program is about 2.5%.

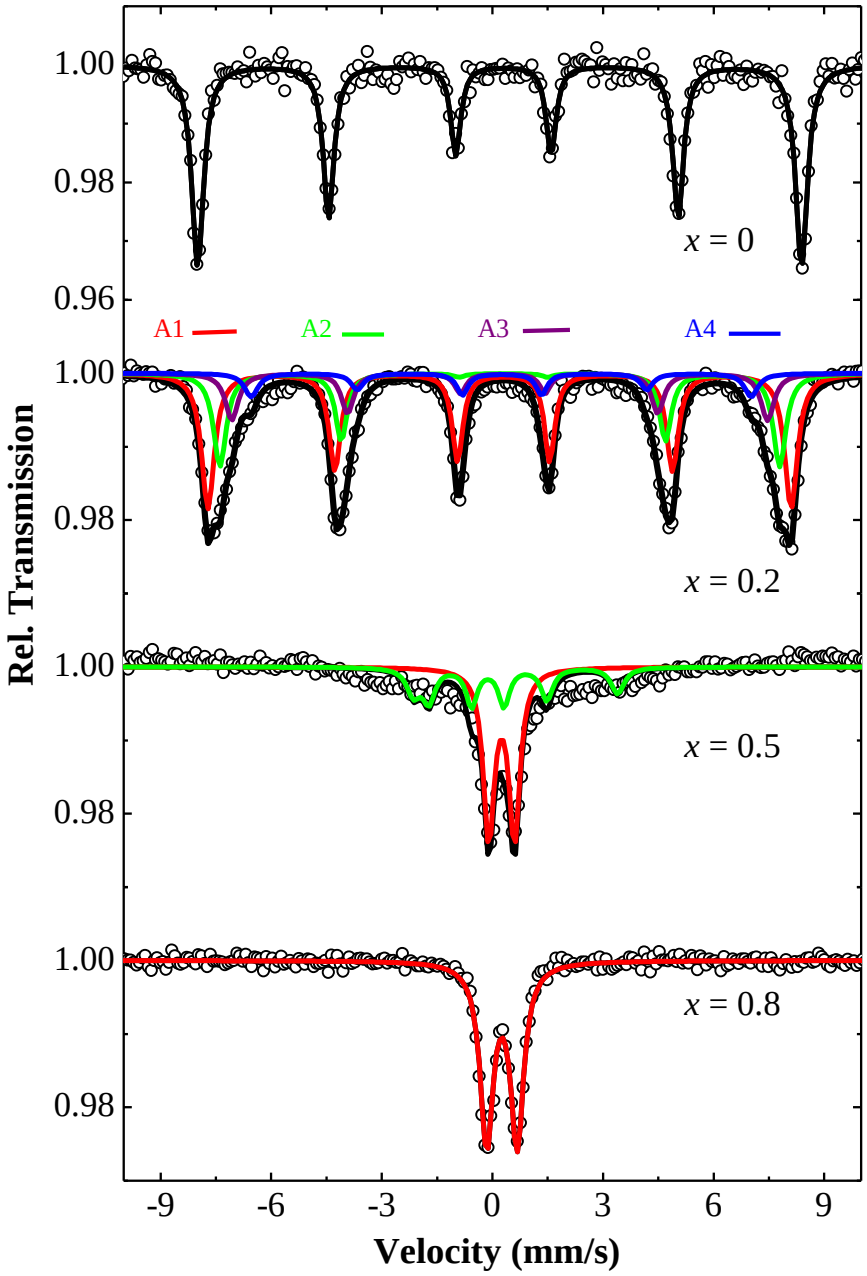


Fig 4.6 : Mössbauer spectra of $SmFe_{1-x}Mn_xO_3$ (x = 0, 0.2, 0.5 and 0.8) measured at 293 K. Solid lines through the data (open circles) is the overall theoretical fit. Overall theoretical fit is derived from the sum of sub-components.

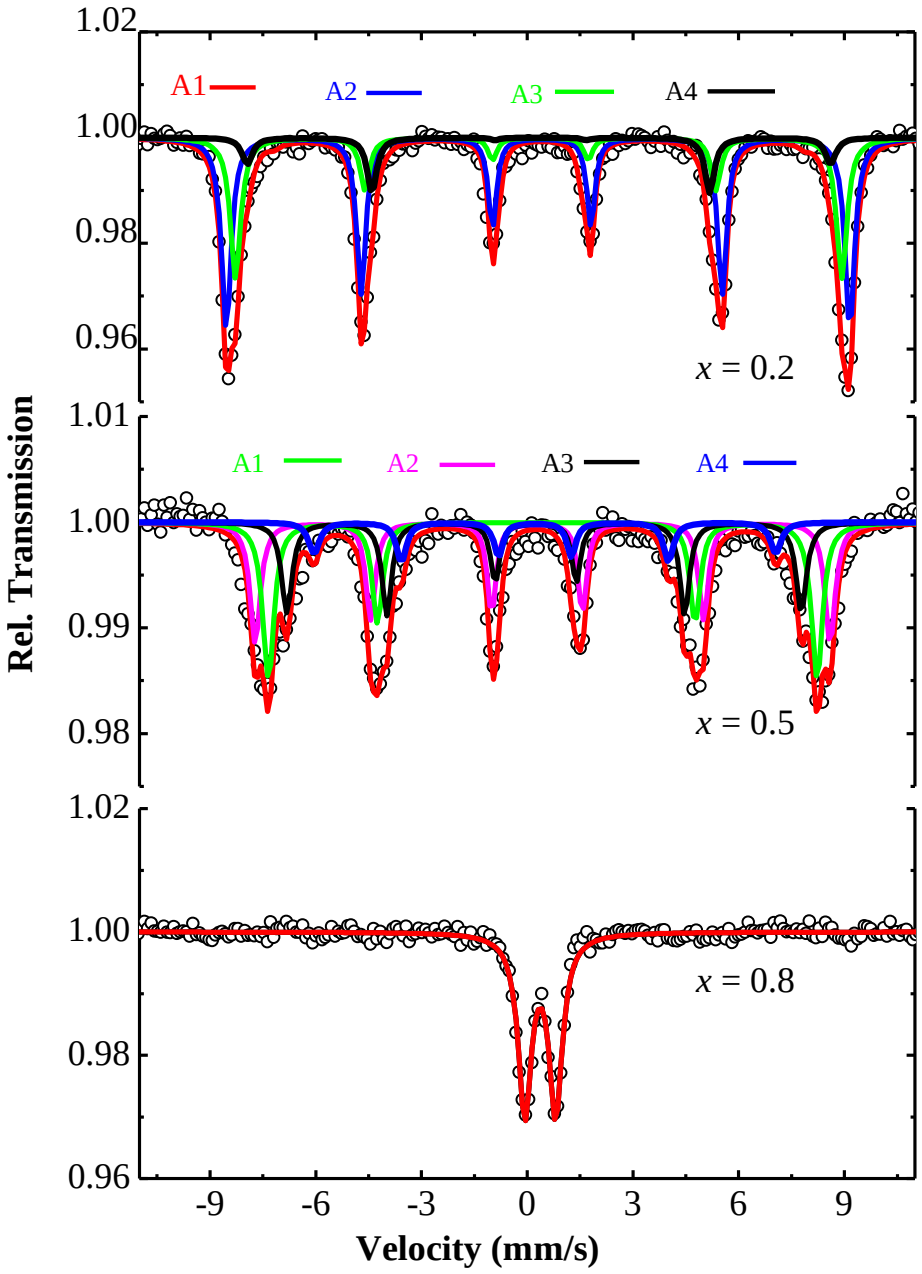


Fig 4.7 : Mössbauer spectra of $SmFe_{1-x}Mn_xO_3$ (x = 0.2, 0.5 and 0.8) measured at 90 K. Solid lines through the data (open circles) is the overall theoretical fit. Overall theoretical fit is derived from the sum of sub-components.

Table 2 : Mössbauer parameters of $SmFe_{1-x}Mn_xO_3$ taken at 293 K.

x	∗δ (mm/s)	QS (mm/s)	Bhf (T)	Γ (mm/s)	E.A. (%)	T.A. (%)	Fe ions
0	0.36	– 0.103	50.8	♦0.32	100	100	6
0.2	0.36	– 0.114	49.1	0.35	42.1	53.4	6
0.2	0.36	– 0.101	47.1	0.35	36.9	33.4	5
0.2	0.35	– 0.0834	45.1	0.36	13.4	11.1	4
0.2	0.36	– 0.0217	42.0	0.37	7.6	2.1	3
0.5	0.36	0.694	–	0.36	61.3	-	-
0.5	0.36	0.75	17.2	0.36	38.7	-	-
0.8	0.38	0.833	–	0.46	100	-	-

Table 3 : Mössbauer parameters of $SmFe_{1-x}Mn_xO_3$ taken at 90 K.

x	∗δ (mm/s)	QS (mm/s)	Bhf (T)	Γ (mm/s)	E.A. (%)	T.A. (%)
0.2	0.47	– 0.103	54.9	0.28	54.7	53.4
0.2	0.46	– 0.0469	53.3	0.30	29.8	33.4
0.2	0.47	– 0.0529	51.3	0.30	11.4	11.1
0.2	0.47	– 0.0270	46.5	0.30	4.1	2.1
0.5	0.47	0.161	50.6	0.30	32.6	10.7
0.5	0.46	0.183	48.3	0.32	30.3	26.8
0.5	0.47	0.237	45.3	0.30	25.8	35.7
0.5	0.47	0.283	40.6	0.31	11.3	26.8
0.8	0.48	0.878	–	∗∗0.46	100	-

♦Indicates the line width is free.

∗ δ is relative to Fe metal.

∗∗ The line width is free.

The Isomer shifts and line widths are fixed unless if indicated.

The spectrum for x = 0.2 was fitted with four magnetic sub-spectra. The Mössbauer spectrum of x = 0.2 shows that the hyperfine field at ^{57}Fe nuclei has a distribution depending on the number n of Mn^{3+} ions on the six nearest neighbor sites of Fe^{3+} ions (Li et al., 1998), (Nishihara, 1975).

From Table 2 it can be seen that the values of the isomer shift (δ) are between 0.35 and 0.38 mm/s for the room temperature measurements. The isomer shift value is consistent with that of the valence of Fe being +3 indicating that it is not affected by the substitution of the Mn ions in the sample. On the other hand the value of the quadrupole splitting (QS) increases from – 0.103 mm/s for x = 0 to 0.833 mm/s for x = 0.8. The QS is proportional to the electric field gradient (EFG) at the Fe nucleus. It can also be seen from Table 3 that the values of QS changes sign from negative (x = 0.2) to positive (x = 0.5) for spectra at 90 K.

The relative abundances obtained from the experimental values at RT and LT are in agreement with the theoretical values for x = 0.2 as indicated in tables 2 and 3. The relative abundance for experimental and theoretical values deviates significantly for x = 0.5. The value of Bhf decreases with increasing Mn content which weakens the magnetic interactions throughout RT and LT series. The substituted Mn ions present in the spectra for x = 0.5 and 0.8 at RT as well as at LT becomes more dominant. The quadrupole interactions in the absence of magnetic field becomes more evident in the sample x = 0.8 both at RT and LT, hence a strong cooperative Jahn-Teller distortion occuring which produces a larger EFG (Jia et al., 1994). This distortion is evident from the large values of QS as indicated in Tables 2 and 3. The spectra of x = 0.5 at LT is fitted with four sextets at 90 K. The sample is paramagnetic at RT and changes to magnetic at 90 K. The values of QS are positive for x = 0.5 (LT) which could be due to a spin reorientation or reorientation of the internal magnetic field with respect to the EFG at Fe site at low temperature (Li et al., 1998).

For the sample with $x = 0.5$, there appears to be an indication of interactions between Fe^{3+} and Mn^{3+} ions present. These interactions lead to competition between cooperative tilt (O-type) and the J-T effect (O′-type) from the MnO_6 octahedra. However the O-type is more dominant in this phase as is evident from the behaviour of the lattice parameters in Table 1. The O′-type distortions start to become dominant as the Mn content increases ($x = 0.8$ and 1). This is clearly evident from the XRD patterns of $x = 0.8$ and $x = 1$ in Fig 4.2. The high value of *QS* for $x = 0.8$ in Tables 2 and 3 seems to confirm a significant presence of J-T distortion (O′-type) in the sample.

4.3 RAMAN SPECTROSCOPY

4.3.1 Surface contamination of pelleted samples and resolution of this problem

The pellets were sintered at 1200°C for 24 hours in air and cooled to room temperature. The sintered pellets had been abraded thoroughly and cleaned with acetone prior to the measurements to remove contamination from the surface of the pellets. The abrading was done using a scalpel applied gently on the surface of the pellet.

The XRD pattern and Raman spectra of the powder resulting from the ground powdered pellet did not show any contamination. There appears to be contamination from the XRD pattern and Raman spectra of the pellets sintered in air. The XRD spectra of $SmFeO_3$ (powder and pellet that was heat treated in air for 24 hours) is shown Fig 4.8. There are some extra peaks from the pattern when the sample was heat treated in air at 1200°C for 24 hours indicating excess oxygen (the contaminant) as shown also in Fig. 4.8. The XRD pattern of pellets sintered at 800°C for 24 hours in Argon did not show any contamination. Hence abrading of the pellets sintered in air

becomes necessary to remove the surface contamination. This surface contamination shows up quite conspicuously in the Raman spectra (not shown). The experimental resolution for all the spectra is 3 cm^{-1}.

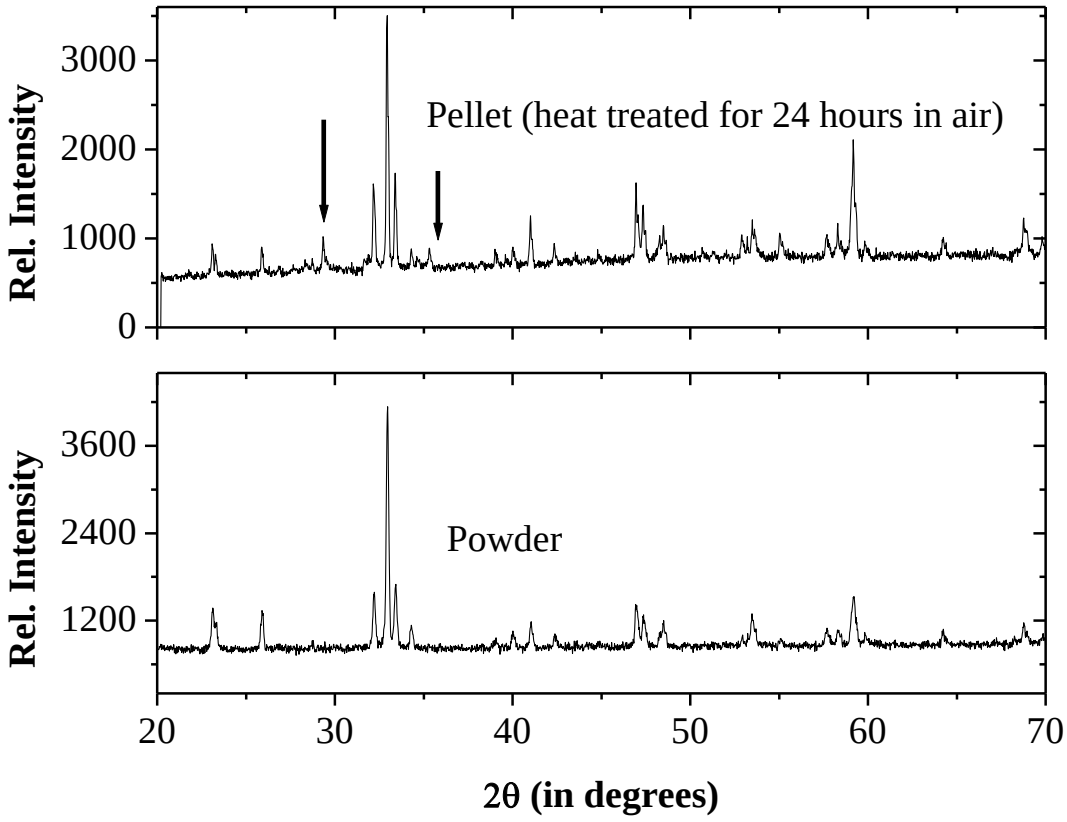


Fig 4. 8 : XRD patterns of $SmFeO_3$ (Pellet and Powder). Arrows show surface contamination peaks in the spectra of the pellets.

Another pellet was prepared from the powder derived from the heat treated pellet. The resulting pellet (Non-sintered) was not heated and Raman measurement was done on it. The sintered pellets were abraded prior to having measurements done on them.

4.3.2 Raman Spectra of all the samples

All the spectra were taken in the cryostat (described in Chapter 3), except for the sintered pellets spectra which were taken outside the cryostat. The spectra for all powders and pellets measured at room temperature and low temperature (77 K) are shown in Figs 4.9 to 4.13.

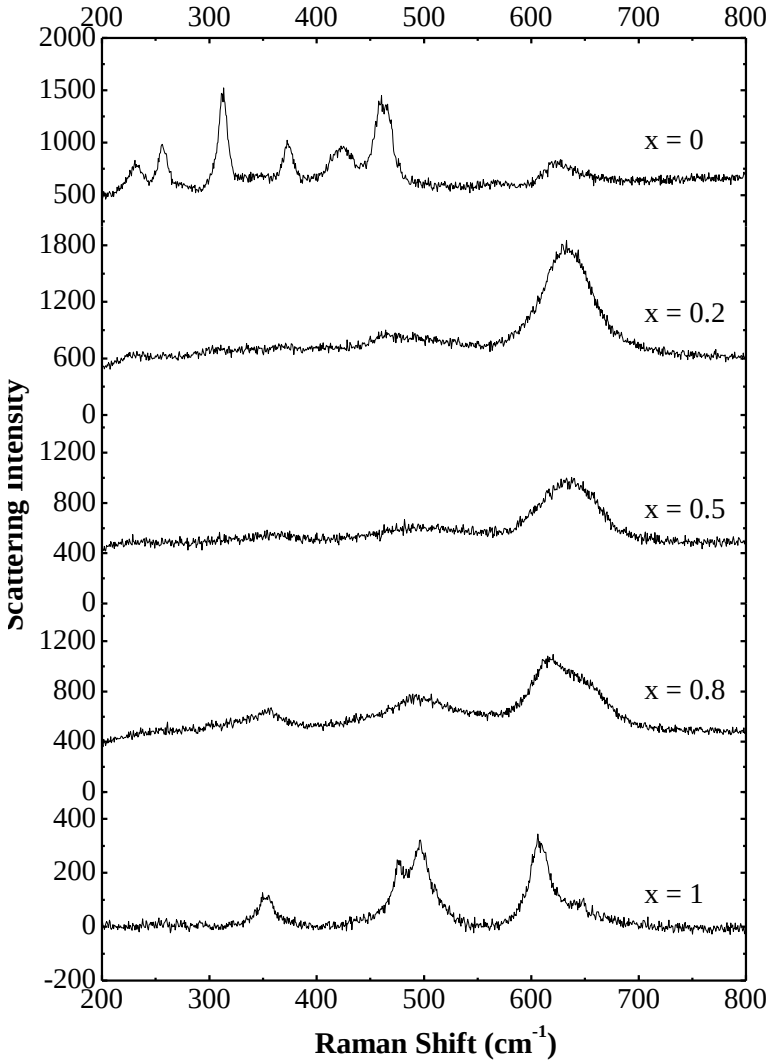


Fig 4.9 : Raman spectra of the powdered samples of $SmFe_{1-x}Mn_xO_3$ at 293 K.

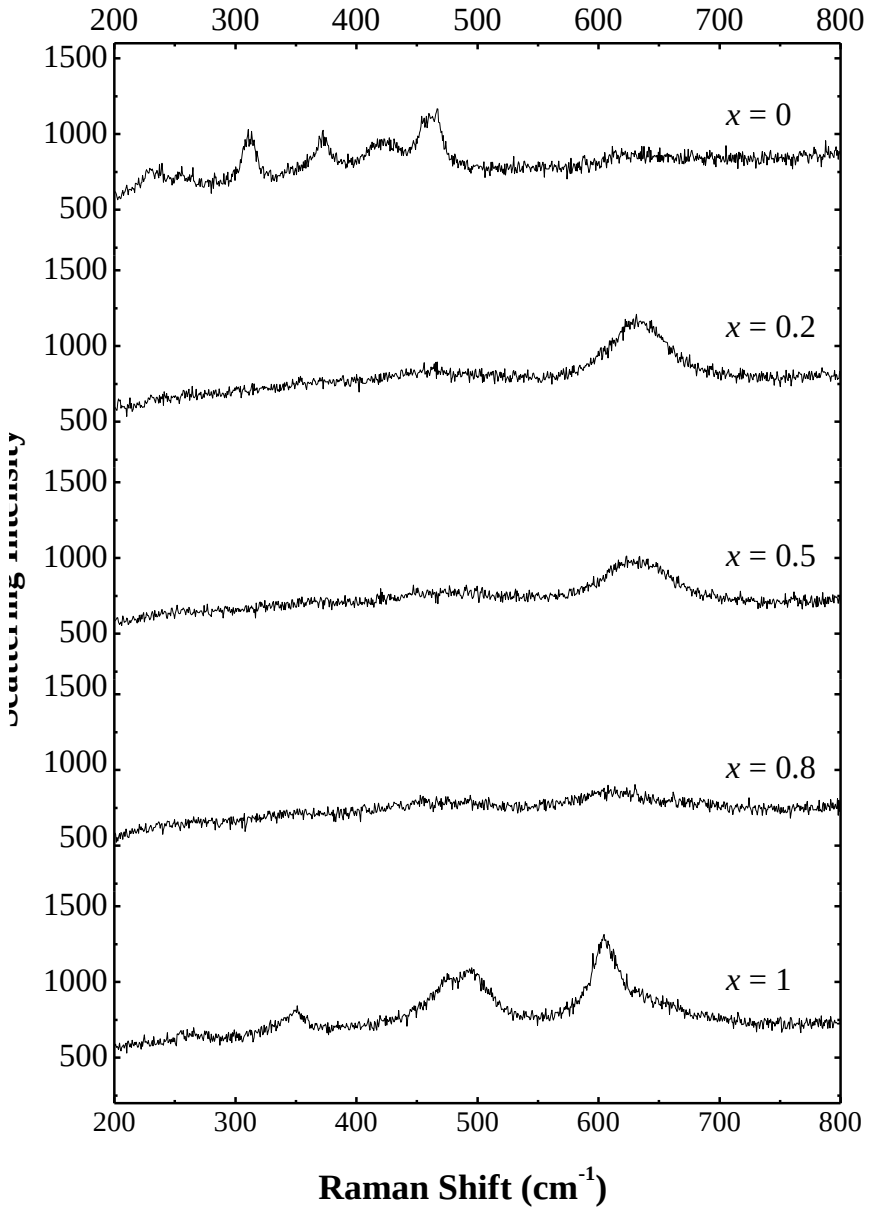


Fig 4.10 : Raman spectra of all the non-sintered pellets of $SmFe_{1-x}Mn_xO_3$ at 293 K.

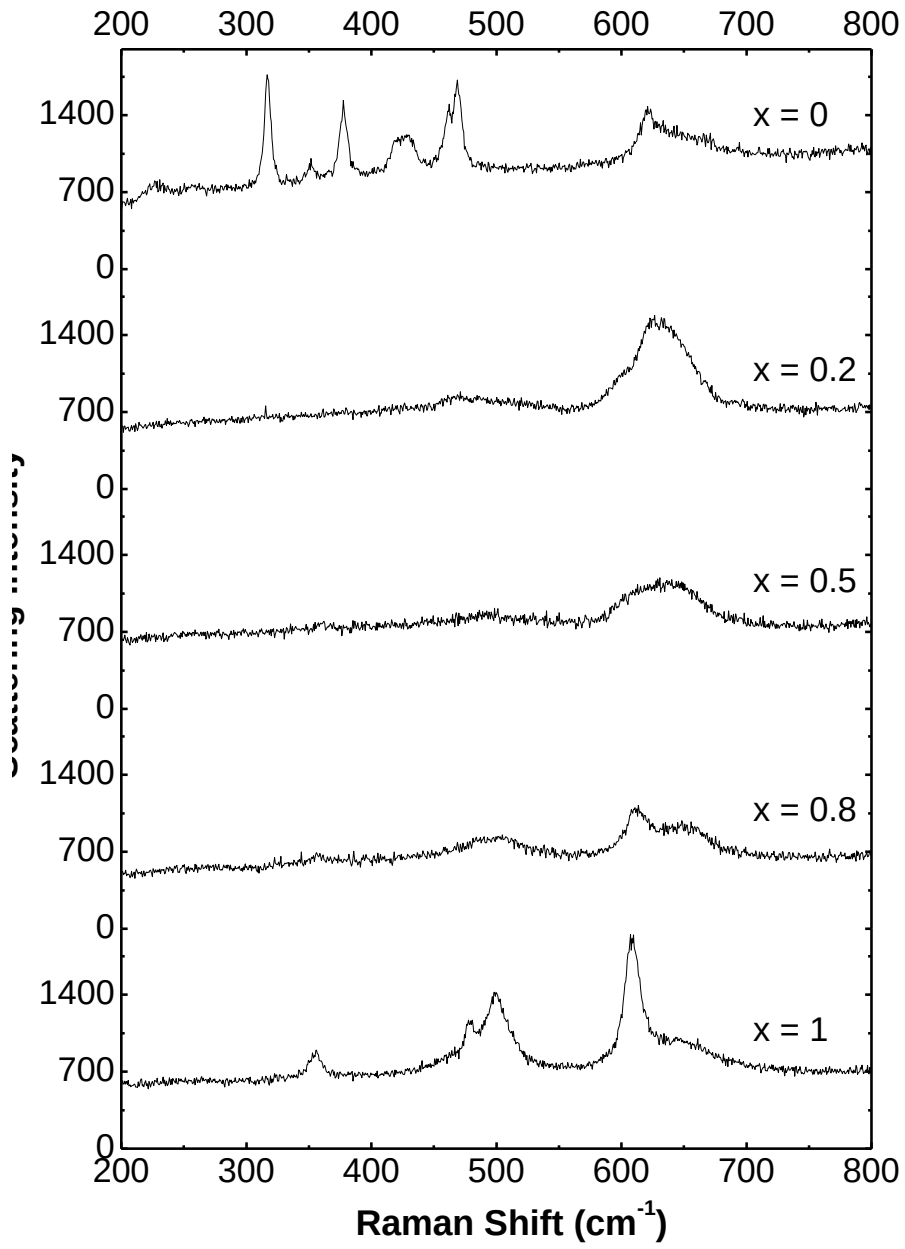


Fig 4.11 : Raman spectra of all the non-sintered pellets of $SmFe_{1-x}Mn_xO_3$ at 77 K.

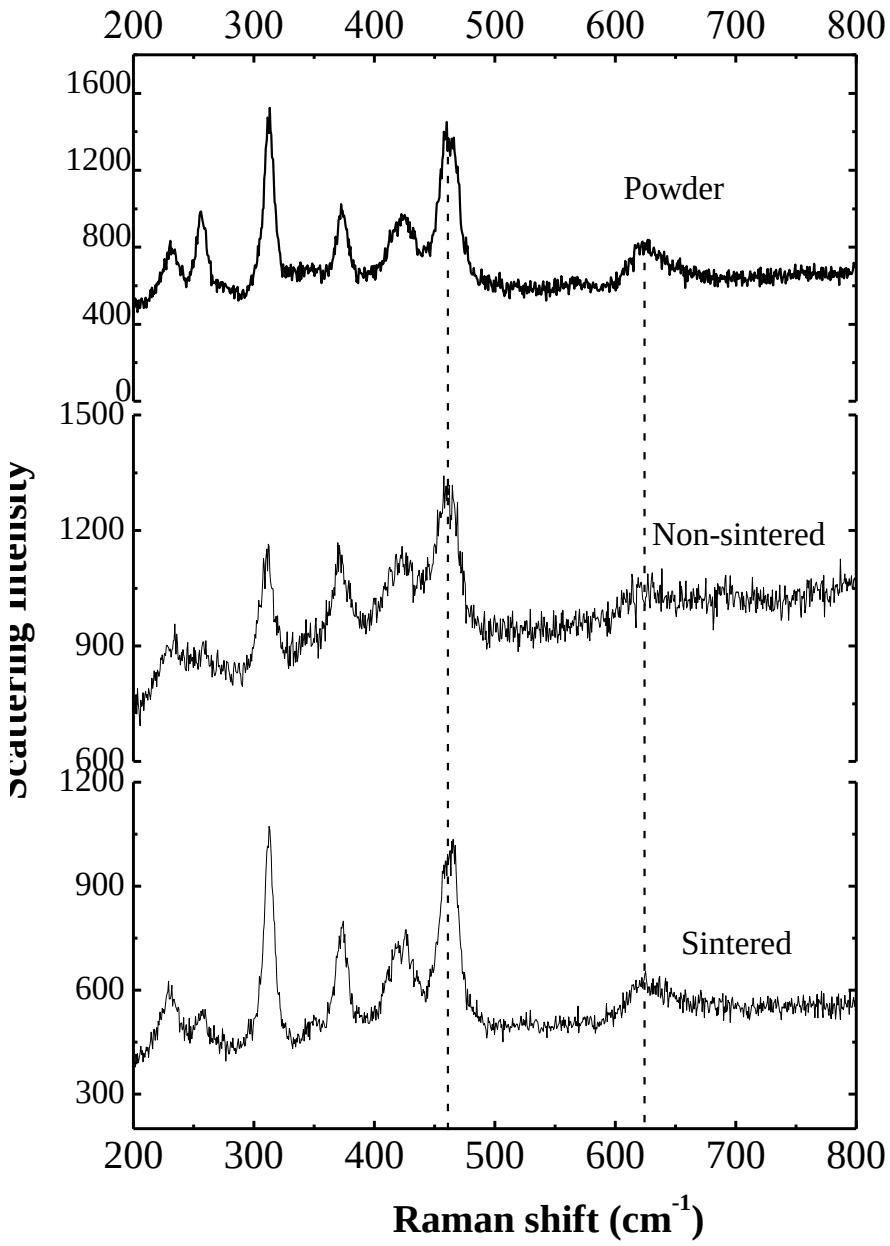


Fig 4.12 : Raman spectra of $SmFeO_3$ (Powder, Non-sintered and Sintered pellet) at 293 K. The dash lines correspond to 480 cm^{-1} and 610 cm^{-1}.

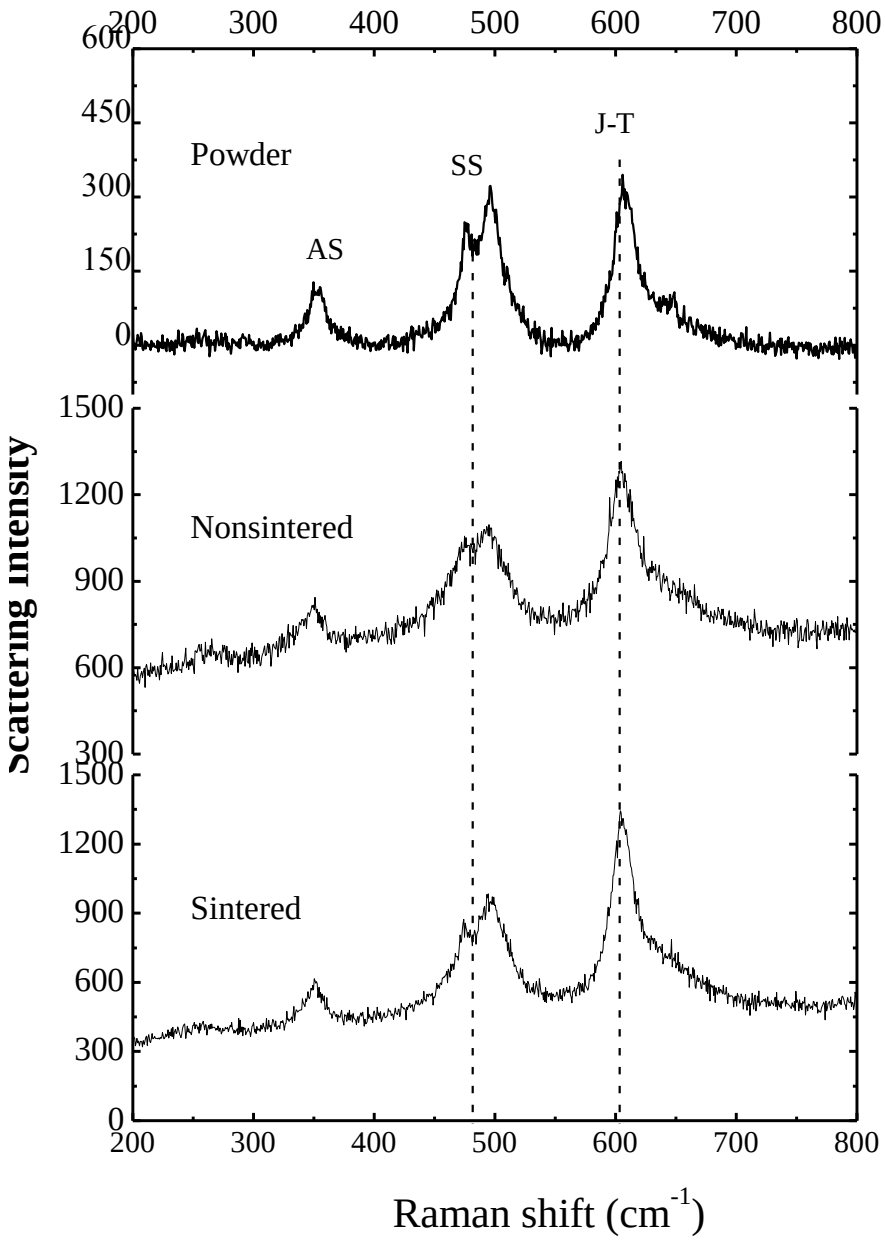


Fig 4.13 : Raman spectra of $SmMnO_3$ (Powder, unsintered and sintered pellet) at 293 K. The dash lines correspond to 480 cm^{-1} and 610 cm^{-1}.

The spectra of the abraded pellets (sintered) and non-sintered pellets (these pellets were compacted from powders and not sintered) compared very well with that of powders at room temperature as indicated in Fig 4.12 and Fig 4.13.

The spectra for $SmFeO_3$ (x = 0) has several peaks at lower energies as shown in Figs 4.9 to 4.11, these are due to the rare earth movements [(Wang et al., 2005), (Martin-Carron et al., 2002) and (Khomskii and Sawatzky, 1997)]. The peaks 480 and 610 cm^{-1} that have been determined to belong to the *Pbnm* orthorhombic structure (Martin-Carron and de Andres, 2001) are present in all the samples (x = 0 to 1) as evident in Figs 4.9 to 4.11.

With the substitution of Mn ions in the sample most of the peaks on the left-hand side of the graph disappear as evident in Figs 4.9, 4.10 and 4.11. When all the Fe ions have been replaced by the Mn ions, three peaks become more prominent in the sample (Fig 4.13). The three peaks are the tilt of the oxygen octahedral, antisymmetric stretching (AS) mode (J-T mode) and symmetric stretching (SS).

Figs 4.14 and 4.15 show the spectrum of $SmMnO_3$ from experiment and Raman normal modes of $RMnO_3$ (Martin-Carron and de Andres, 2001), respectively showing the three prominent features.

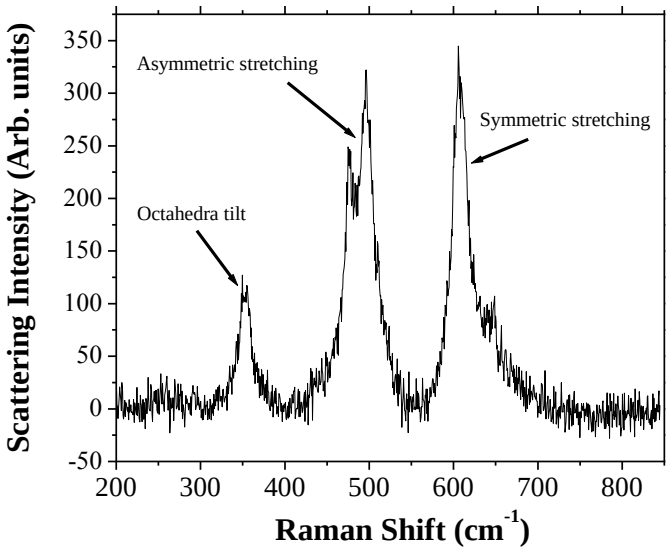


Fig 4.14 : Raman Spectrum of $SmMnO_3$ at 293 K.

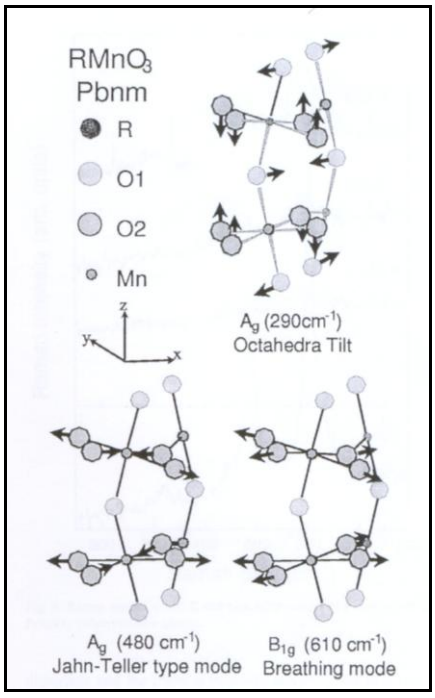


Fig 4.15 : Raman normal modes of $RMnO_3$ in the *Pbnm* structure (Martin-Carron and de Andres, 2001).

The peak around 632 cm^{-1} (symmetric stretching) is present throughout the spectra for all the samples (x = 0, 0.2, 0.5, 0.8 and 1). As the content of Mn ions increases in the room temperature series so does the intensity of the AS mode. This mode is associated with J-T distortion. This distortion increases and is more noticeable for x = 0.8 and x = 1.

Lowering the temperature does not change the Raman spectra significantly as evident in Figs 4.10 and 4.11, it only sharpens the peaks at 77 K. The distortion does not change the lattice crystallographic symmetry but modifies the structure [(Li et al., 1998), (Khomskii and Sawatzky, 1997)] as is evident in the changes of the lattice parameters (Fig 4.2).

4.4 MAGNETIZATION MEASUREMENTS

The temperature dependence of the magnetization curves of $SmFe_{1-x}Mn_xO_3$ (x = 0.2, 0.5, 0.8 and 1) are shown in Figs 4.16, 4.17, 4.18 and 4.19 under an applied field H = 50 Oe FC (Field cooling) experiments. Field cooled (FC) is where a magnetic field is applied well above T_C to the sample and cools it in the field down to $T \ll T_C$, all the while recording the magnetization while ZFC is where the sample is first cool to zero field from $T \gg T_C$ down to $T \ll T_C$. At low temperature, a field is applied and the sample is heated while measuring the magnetization up to $T > T_C$ with the field constant.

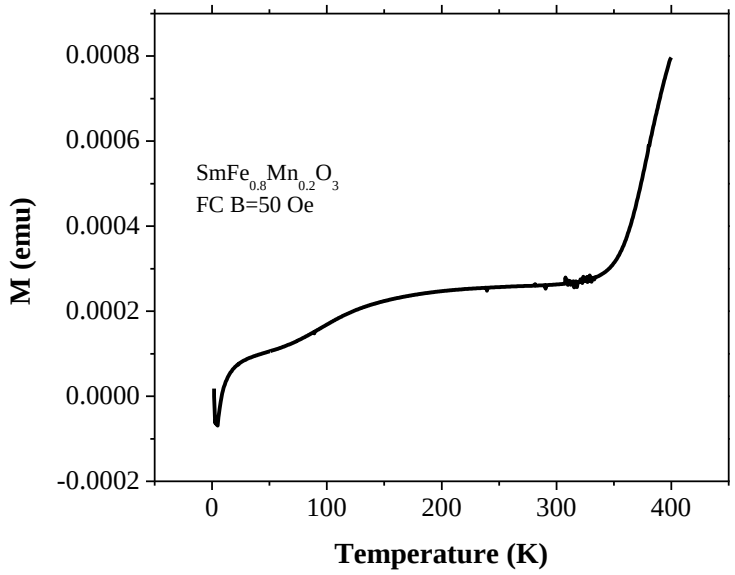


Fig 4.16 : Temperature dependence of magnetization of $SmFe_{0.8}Mn_{0.2}O_3$ in applied field of 50 Oe.

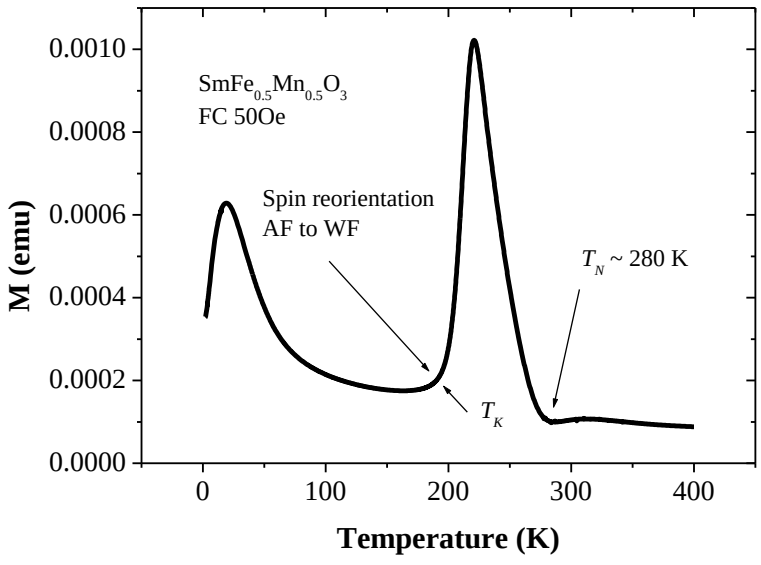


Fig 4.17 : Temperature dependence of magnetization of $SmFe_{0.5}Mn_{0.5}O_3$ in applied field of 50 Oe.

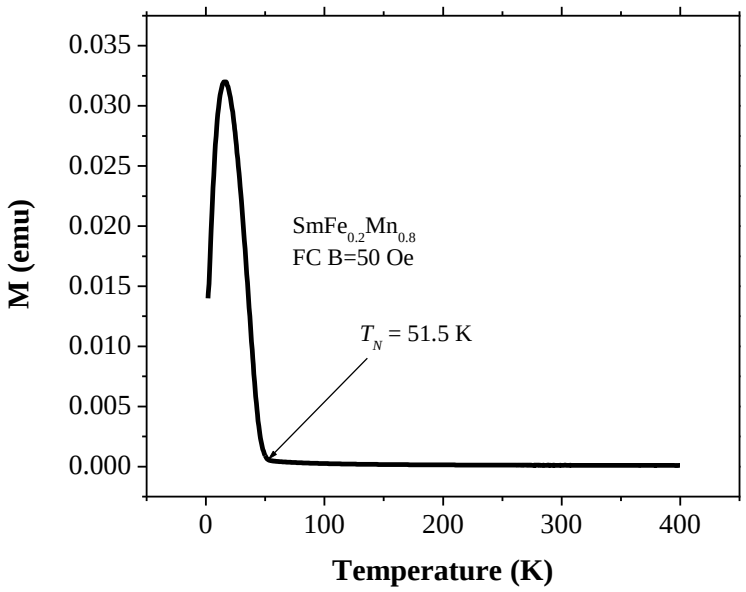


Fig 4.18 : Temperature dependence of magnetization of $SmFe_{0.2}Mn_{0.8}O_3$ in applied field of 50 Oe.

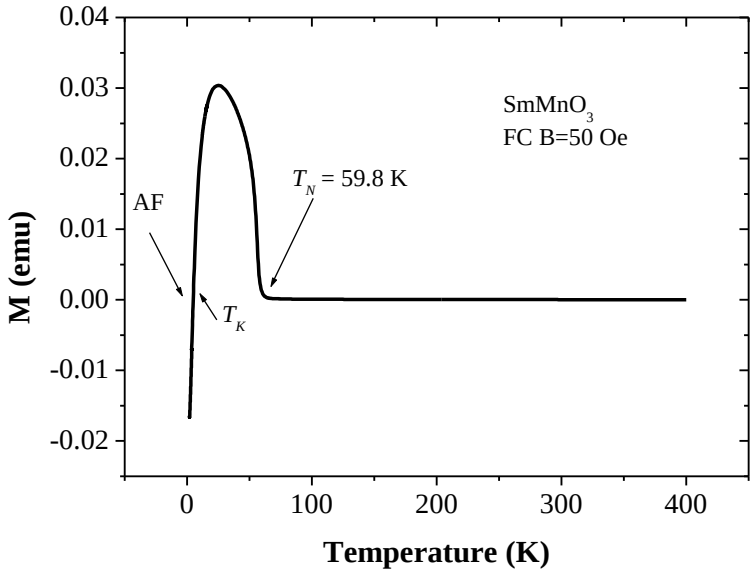


Fig 4.19 : Temperature dependence of magnetization of $SmMnO_3$ in applied field of 50 Oe.

T_N (Neel Temperature) (the temperature where the system starts to become magnetically ordered) is identified from where the magnetic moments start to change precipitously as indicated in Fig 4.17. T_K (the onset temperature where antiferromagnetic spins tilt slightly to become weakly ferromagnetic) is identified by a less dramatic kink in the temperature dependence of magnetic moment at some temperature below T_N (Bouziane et al., 2005). Hence T_K is the temperature at which transition takes place from weak ferromagnetism (WF) to antiferromagnetism (AF) also indicated in Fig 4.17.

From the temperature dependence of the magnetization graphs above the following are deduced:

- The spin reorientation temperature T_K (where there is a re-orientation of the 3d spin sub-lattice) is not well established for the sample with x = 0.2, this is in agreement with what was reported in the literature (Bouziane et al., 2005) as indicated in Fig 4.16. There is a competition between weak ferromagnetism (WF) and antiferromagnetism (AF) orderings below ~ 350 K (Bouziane et al., 2005), (Nagata et al., 2001).
- In the Mn-rich series T_K is well established only for the sample with x = 0.5 ($T_K \approx$ 200 K) as shown also in Fig 4.17. From the figure it is observed that the spin orientation T_K ~ 185 K and then WF takes over below this temperature. This could be due to the interactions between Mn^{3+} and Fe^{3+} ions. There may be different pairing interactions coexisting such as $Fe^{3+} - Fe^{3+}$, $Mn^{3+} - Fe^{3+}$ and $Mn^{3+} - Mn^{3+}$ in the sample. If one assumes that there are equal numbers of Mn^{3+} and Fe^{3+} ions in the sample then the competition between them may have result in this behavior as seen in Fig 4.17. The WF is as a result of the Fe 3d spin structure in the lattice. It has been reported that the WF is as result of spin canting from the ideal Fe 3d two-sub lattice antiferromagnetic ordering (Bouziane et al., 2005). This interaction from low temperature AF to high temperature WF phases was also observed in other non-magnetic rare earth orthoferrites as $YFe_{1-x}Mn_xO_3$ as well (Nagata et al., 2001).
- The spin-reorientation transition is caused by an alteration in and competition between the various super exchange interactions (Nagata et al., 2001). Such a

spin-reorientation transition is the change from weak ferromagnetism to antiferromagnetism in the sample as a result of the increase in the Mn content.

- In the Mn-rich series T_K appears only for $x = 0.5$, this seems to be the critical concentration where Mn starts to play a dominant role in determining the spin configuration for $SmFe_{1-x}Mn_xO_3$ (Nagata et al., 2001).
- When Fe ions are replaced by Mn ions in $SmFeO_3$, T_K decreases monotonically as the Mn content increases (Nagata et al., 2001), (Bouziane et al., 2005).
- T_K decreases with increasing Mn content ($x = 0.5$ to $x = 1$), this could be because of the interaction between Mn^{3+} and Fe^{3+} ions (Bouziane et al., 2005).
- The substitution of Fe ions by Mn ions weakens the AF interaction of Fe^{3+} - Mn^{3+} (Bouziane et al., 2005).
- T_N was not observed for $x = 0.2$ as shown in Fig 4.16, but is expected to be above room temperature at ~ 400 K (Bouziane et al., 2005).
- T_N was observed for $x = 0.8$ and 1 as shown in Figs 4.18 and 4.19 respectively.

The temperature dependence of the zero field-cooled (ZFC) magnetization measurements for $SmFe_{1-x}Mn_xO_3$ ($x = 0.2$ and 0.5) under an applied field $H = 50$ Oe are shown in Figs 4.20 and 4.21, respectively. The temperature dependence of the ZFC magnetization measurements for $x = 1$ under an applied field of $H = 10$ Oe is shown in Fig 4.22.

These physical significance of the change between 10 K up to 60 K in Fig 4.22 is still not well understood.

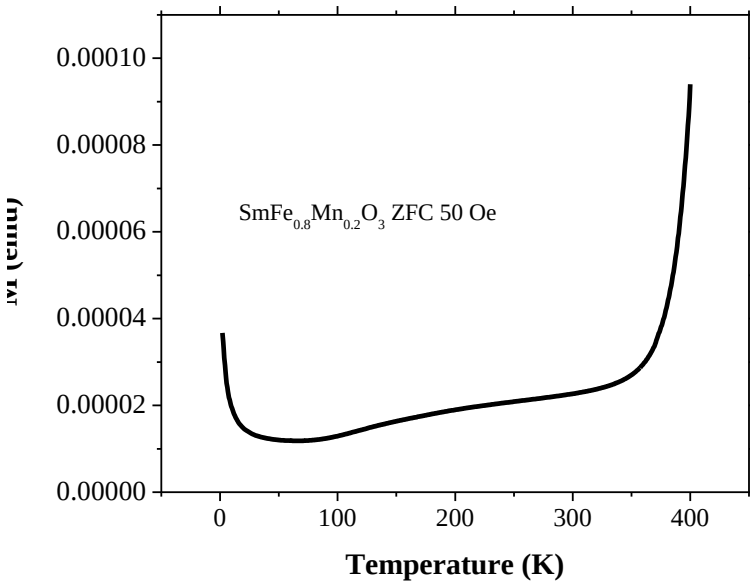


Fig 4.20 : Temperature dependence of magnetization of $SmFe_{0.8}Mn_{0.2}O_3$ in applied field of 50 Oe.

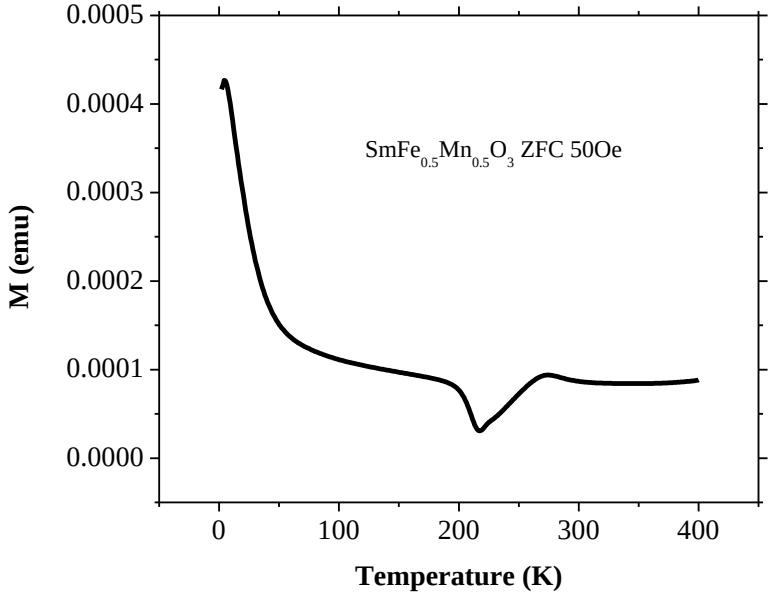


Fig 4.21 : Temperature dependence of magnetization of $SmFe_{0.5}Mn_{0.5}O_3$ in applied field of 50 Oe.

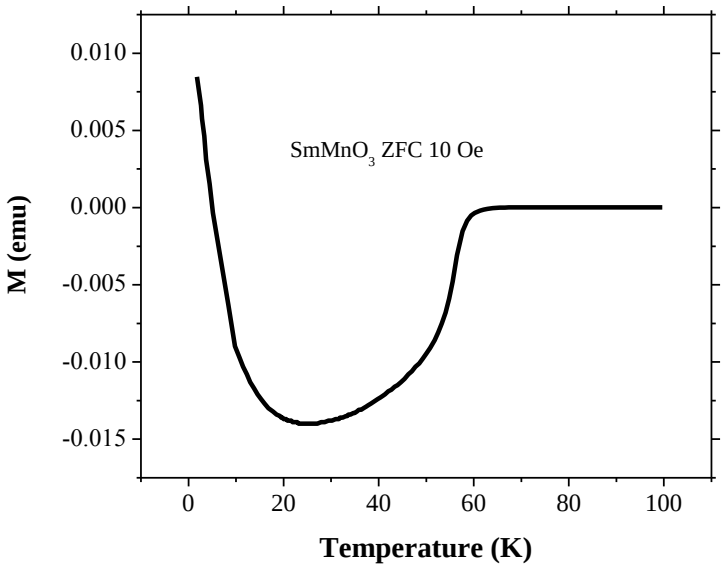


Fig 4.22 : Temperature dependence of magnetization of $SmMnO_3$ in applied field of 10 Oe.

Fig 4.23 shows the graph of T_N versus Mn content; Fig 4.24 is the graph of T_K versus the Mn and Fig 4.25 the graph of T_N versus the unit volume for $SmFe_{1-x}Mn_xO_3$ (x = 0, 0.2, 0.5, 0.8 and 1), respectively.

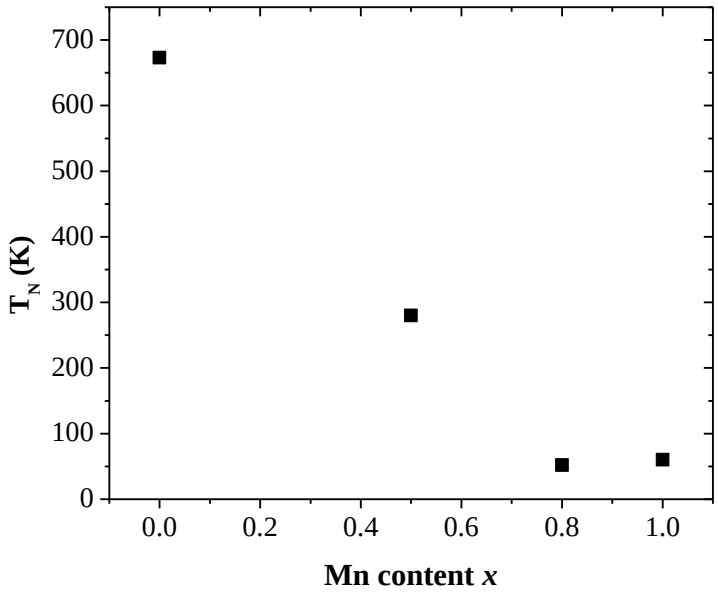


Fig 4.23 : Mn content dependence of Neel Temperature (T_N) of $SmFe_{1-x}Mn_xO_3$.

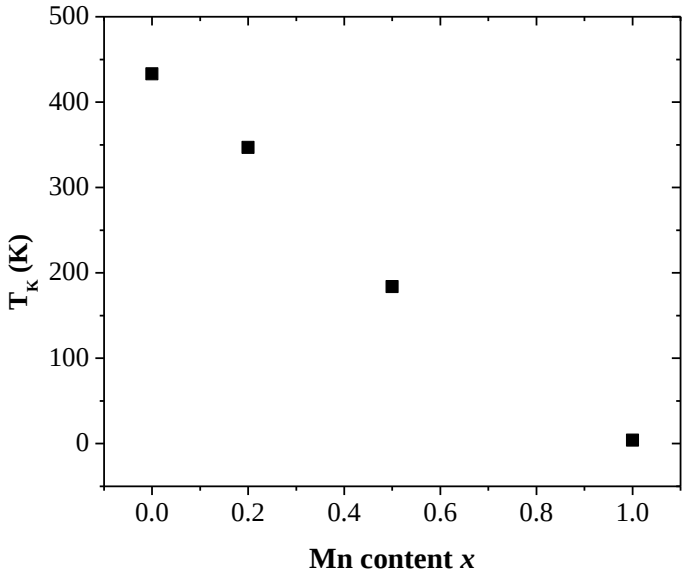


Fig 4.24 : Mn content dependence of Transition Temperature (T_K) of $SmFe_{1-x}Mn_xO_3$.

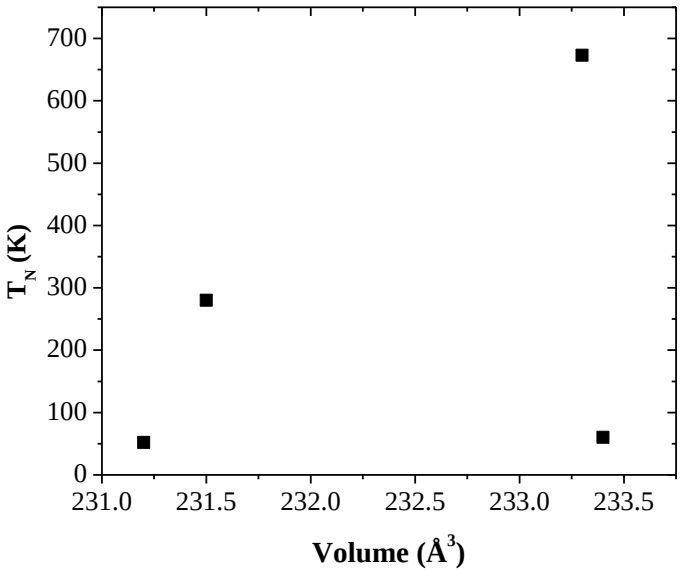


Fig 4.25 : Volume dependence of Neel Temperature of $SmFe_{1-x}Mn_xO_3$.

Figs 4.23 and 4.24 clearly show that as the Mn content increases both T_K and T_N decreases. The decrease may be attributed to the distortion taken place as a result of the increased Mn ions present in the sample. The electronic structure of Mn^{3+} and Fe^{3+} are different, the magnetic moment of Mn is is smaller than that of Fe (Bouziane et al., 2005), (Nagata et al., 2001) as well as having a smaller spin structure may have contributed to this.

Fig 4.25 shows that the average volume of the unit cell which increases with Neel temperature and can be attributed to the increase in Mn^{3+} ions in the sample.

CHAPTER 5

CONCLUSIONS

The objectives set out for this project were to synthesise and characterize Mn-doped $SmFeO_3$ ($SmFe_{1-x}Mn_xO_3$ where x = 0, 0.2, 0.5, 0.8 and 1) in order to check the effects of doping on the magnetic and electronic properties have been achieved.

All the samples of $SmFe_{1-x}Mn_xO_3$ (x = 0, 0.2, 0.5, 0.8 and 1) were found to be single perovskite phases. The lattice parameters a and c decrease while the lattice parameter b increases with increased Mn content. The average unit cell volume V is constant. The change in the lattice constants indicates that the substitution of Mn induces a distortion in the crystal lattice of $SmFeO_3$. There is a considerable distortion as evident from the changes in the lattice parameters in the crystal lattice of $SmFe_{1-x}Mn_xO_3$. The degeneracy of the orbital doublet of the octahedral crystal-field is expected to be lifted by the deformation of the lattice. Both the tilting and distortion of the FeO_6 octahedron increases with the increase of the Mn content and this also has an effect on the O-Mn-O angles of the octahedra.

The pattern strain parameter s increases upon increasing Mn doping for two reasons; the octahedral tilting and the distortion of the MnO_6 octahedra due to the orbital ordering characteristic of the Jahn-Teller (J-T) effect of Mn^{3+} ions (Alonso et al., 2000). This is evident from the XRD pattern of the sample x = 1 showing well-defined reflections as all the Fe ions have been replaced by Mn ions.

During the sintering process of the pelleted samples in air, there appears to be surface contamination as a result of excess oxygen. This was evident from the XRD pattern of the pellet that was heat treated in air for 24 hours. This contamination can be removed by abrading the surface of the sintered pellet. One should be aware of the

contamination effects from the sintering process, especially in the case of sensitive magnetic characterisation of small magnetic moment contributions.

Mössbauer measurements show that, for $x \geq 0.5$, the Jahn-Teller distortion increases, resulting in a large EFG. Hence a large *QS* is observed for $x = 0.5$ and 0.8. The increase in the value of *QS* may be attributed to the lattice distortion as well as the distortion of the Fe local environment due to the J-T effect. The values of the isomer shift are fairly constant for RT or LT series. It has been reported that in perovskites containing trivalent Fe and Mn, the energy of the crystal field splitting is smaller than Hunds energy between two electrons (Li et al., 1998) and the references therein. So the Fe and Mn ions are in the high-spin state. The distribution of the hyperfine field is due to the effect of the nearest neighbour Mn cations (disorder). The relative area of the sub-spectra is proportional to the population of Fe ions at a given site of the lattice (for x = 0.2 at both RT and LT and 0.5 LT) in a particular local environment with certain set on Mn nearest neighbours. The Mössbauer results show that there is a random distribution of Mn in the sample and this is according to comparison with the binomial distribution theory.

The Raman spectra show that there is a disorder in the vibrational bands with increasing Mn content. This is because most of the Raman modes below 600 cm^{-1} are suppressed by the substitution of Mn ions ($x = 0.2$, 0.5 and 0.8) and the only mode visible throughout the series is the J-T mode. Only three modes are prominent when all the Fe ions have been replaced by Mn ions ($x = 1$), showing the effect of the disorder.

The interaction between Fe^{3+} and Mn^{3+} seem to be the cause for the decrease in T_N as both T_N and T_k decrease with an increase in the Mn content. This was similar to what was reported in literature (Bouziane et al., 2005). The spin reorientation transition is caused by a change in the superexchange interaction between Fe^{3+} and Mn^{3+}. The

structure of the spin sub-lattice appears to be affected by the contribution of Mn^{3+} ions substituted in the lattice of $SmFeO_3$.

From the discussion, it can be concluded that the substitution of Mn ions in $SmFeO_3$ not only weakens the exchange interaction and reduces the Curie temperature, but also induces a J-T distortion which results in a large electric field gradient at the ^{57}Fe nucleus. The crystallographic structure of the sample is modified by the substitution of Mn ions (Li et al., 1998) because the atomic radii of Fe^{3+} and Mn^{3+} in $SmFe_{1-x}Mn_xO_3$ (x = 0. 0.2, 0.5, 0.8 and 1) are very similar (De et al., 2005). Hence the double exchange interaction between Fe^{3+} and Mn^{3+} occur in $SmFe_{1-x}Mn_xO_3$ because Fe^{3+} and Mn^{3+} have the same electronic structure.

The samples were prepared in small quantities (~ 15 mg) and a magnetic characterization was performed fully by a combination of techniques after having established reliable synthesis and characterisation procedures of these compounds mentioned above. This is for future high pressure ^{57}Fe Mössbauer studies in the diamond-anvil-cell (DAC) where all the samples will have to be prepared in ^{57}Fe enriched form in very small quantities of mg. In addition a preliminary magnetic characterisation of the full series extending on the previous work of (Bouziane et al., 2005) for the Fe-rich only ($SmFe_{1-x}Mn_xO_3$ where x = 0.7, 0.8 and 0.9) was done.

This work now forms a stepping stone for envisaged future work involving high pressure studies of these compounds in order to see how the magnetic-electronic properties can be altered by pressure.

REFERENCES

ALONSO, J. A., MARTINEZ-LOPE, M. J. & CASAIS, M. T. (2000) Evolution of the Jahn-Teller Distortion of MnO_6 Octahedra in $RMnO_3$ Perovskites (R=Pr, Nd, Dy, Tb, Ho, Er, Y): A Neutron Diffraction Study. *Inorg. Chem.,* 39**,** 917-923.

BASHKIROV, S. S., PARFENOV, V. V., ABDEL-LATIF, I. A. & ZARIPOVA, L. D. (2005) Mossbauer effect and electrical properties studies of $SmFe_xMn_{1-x}O_3$ (x=0.7, 0.8 and 0.9). *Journal of Alloys and Compounds* 387**,** 70-73.

BOUZIANE, K., YOUSIF, A., ABDEL-LATIF, I. A., HRICOVINI, K. & RICHTER, C. (2005) Electronic and magnetic properties of $SmFe_{1-x}Mn_xO_3$ orthoferrites (x=0.1, 0.2 and 0.3). *Journal of Applied Physics,* 97**,** 10A504.

CARROTA, M. C., BUATRRURI, M. A., MARTINELLI, G., SADAOKA, Y., NUNZIATE, P. & TRAVERSA, E. (1997) *Sens. Actuators,* B 44**,** 590-594.

CARROTA, M. C., MARTINELLI, G., SADAOKA, Y., NUNZIANTE, P. & TRAVERSA, E. (1998) *Sens. Actuators,* B 48**,** 270-276.

CHERRY, M., ISLAM, M. S. & CATLOW, C. R. A. (1995) *Journal of Solid State Chemistry,* 118.

CHERRY M., I., M.S., CATLOW, C.R.A. (1995) *Journal of Solid State Chemistry*, 118.

CIAMBELLI, P., CIMINO, S., DE ROSSI A., FATICANTI, M., LISI, L., MINELLI, G., PETTITI, I., PORTA, P., RUSSO, G., TURCO, M. (2000) $AMnO_3$ (A=La, Nd, Sm) and $Sm_{1-x}Sr_xMnO_3$ perovskites as combustion catalysts: structural, redox and catalytic properties. *Applied Catalysis B: Environmental*, 24**,** 243 - 253.

COELHO, A. A. (2003) Topas. 3.1 ed., Bruker AXS GmbH, Karlsruhe, Germany.

CONVERT, F. & MIEGE, B. (1992) The Control of Geometrical Sources of Error in X-ray Diffraction Applied to Stress Analysis. *Journal of Applied Crystal,* 25**,** 384.

DE, K., RAY, R., PANDA, R. N., GIRI, S., NAKAMURA, H. & KOHARA, T. (2005) The effect of Fe substitution on magnetic and transport properties of $LaMnO_3$. *Journal of Magnetism and Magnetic Materials,* 288**,** 339-346.

EIBSCHUTZ, M., GORODETSKY, G., SHTRIKMAN, S. & TREVES, D. (1964) Differential Thermal Analysis and Mossbauer Studies in Rare-Earth Orthoferrites. *Journal of Applied Physics,* 35**,** 1071-1072.

EIBSCHUTZ, M., SHTRIKMAN, S. & TREVES, D. (1967) Mossbauer Studies of Fe^{57} in Orthoferrites. *Physical Review,* 156**,** 562-577.

GIBB, T. C. (1983a) Magnetic Exchange Interaction in Perovskite Solid Solutions. Part 2. Iron-57 and ^{151}Eu Mossbauer Spectra of $EuFe_{1-x}Mn_xO_3$ ($0<x<1$). *J. Chem. Soc. Dalton Trans.*

GIBB, T. C. (1983b) Magnetic Exchange Interactions in Perovskite Solid Solutions. Part 1. Iron-57 and ^{151}Eu Mossbauer Spectra of $EuFe_{1-x}Co_xO_3$ ($0<x<1$). *J. Chem. Soc. Dalton Trans.*

GUTLICH, P., LINK, R. & TRAUTWEIN, A. (Eds.) (1978) *Mössbauer Spectroscopy and Transition Metal Chemistry*, Springer, Berlin.

ILIEV, M. N. & ABRASHEV, M. V. (2001) Raman phonons and Raman Jahn-Teller bands in perovskite-like manganites. *Journal of Raman Spectroscopy,* 32**,** 7.

ILIEV, M. N., ABRASHEV, M. V., LEE, H. G., POPOV, V. N., SUN, Y. Y., THOMSEN, C., MENG, R. L. & CHU, C. W. (1998) Raman spectroscopy of orthorhombic perovskitelike $YMnO_3$ and $LaMnO_3$. *Physical Review B,* 57.

JIA, Y. Q., LIU, S. T., WU, Y., JIN, M. Z., LIU, X. W. & LIU, M. L. (1994) Crystal Structures and Mossbauer Spectra of $LaFe_{1-x}Mn_xO_3$ and $LaFe_{1-x}Co_xO_3$ (x=0 to 0.9). *Phys. Stat. Sol.,* 143**,** 15-22.

KHOMSKII, D. (2001) Electronic Structure, Exchange and Magnetism in Oxides. IN THORNTON, M. J. & ZIESE, M. (Eds.) *Lecture Notes in Physics 569.*

KHOMSKII, D. I. & SAWATZKY, G. A. (1997) Interplay between spin, charge and orbital degrees of freedom in magnetic oxides. *Solid State Communications,* 102**,** 87-89.

KIM, S., DEMAZEAU, G., PRESNIAKOV, I. & CHOY, J. (2001) Structural Distortion and Chemical Bonding in $TlFeO_3$: Comparison with $AFeO_3$ (A=Rare Earth). *Journal of Solid State Chemistry,* 161**,** 197-204.

LI, L., SONG, X., SU, W., WEI, Q. & KANG, Z. (1998) The influence of substitution of Mn ions on quadrupole splitting of $EuFeO_3$ perovskite oxide. *Hyperfine Interactions,* 116**,** 167-172.

LONG, D. A. (Ed.) (2002) *The Raman Effect A Unified Treatment of the Theory of Raman Scattering by molecules,* John Wliey & sons, Ltd.

LONG, G. J., CRANSHAW, T. E. & LONGWORTH, G. (1983) The ideal Mössbauer effect absorber thickness *Mössbauer Effect Reference and Data,* 6**,** 42.

MAREZIO, M., REMEIKA, J. P. & DERNIER, P. D. (1970) The Crystal Chemistry of the Rare Earth Orthoferrites. *Acta Cryst.,* B26**,** 2008-2029.

MARTIN-CARRON, L. & DE ANDRES, A. (2001) Raman phonons and Jahn-Teller transition in $RMnO_3$ manganites. *Journal of Alloys and Compounds,* 323-324**,** 5.

MARTIN-CARRON, L., DE ANDRES, A., MARTINEZ-LOPE, M. J., CASAIS, M. T. & ALONSO, J. A. (2002) Raman phonons as a probe disorder, fluctuations, and local structure in doped and undoped orthorhombic and rhombohedral manganites. *Physical Review B,* 66**,** 8.

MARTINELLI, G., CARROTA, M., FERRONI, M., SADAOKA, Y. & TRAVERSA, E. (1999) *Sens. Actuators,* B 55**,** 99-110.

MASLEN, E. N., STRELTSOV, V. A. & ISHIZAWA, N. (1996) A Synchrotron X-ray Study of the Electron Density in $SmFeO_3$. *Acta Cryst.,* B52.

MAY, L. (Ed.) (1971) *An Introduction to Mössbauer Spectroscopy*, Plenum Press.

MCKIE, D. & MCKIE, C. (Eds.) (1992) *Essentials of Crystallography,* Blackwell Scientific Publications.

MINH, N. Q. (1993) *Journal of American Ceramic Society,* 76**,** 563 - 568.

MURAD, E. & CASHION, J. (Eds.) (2004) *Mössbauer Spectroscopy of Environmental Minerals and their Utilization,* Kluwer Academic.

NAGATA, Y., YASHIRO, S., MITSUHASHI, T., KORIYAMA, A., KAWASHIMA, Y. & SAMATA, H. (2001) Magnetic properties of $RFe_{1-x}Mn_xO_3$ (R=Pr, Gd, Dy). *Journal of Magnetism and Magnetic Materials* 237**,** 250-260.

NISHIHARA, Y. (1975) Effect of Nearest Neighbor Ions on the Hyperfine Fields at ^{57}Fe in $TbFe_{1-X}Cr_xO_3$. *J. Phys. Soc. Jpn.,* 38.

NISHIHATA, Y., MIZUKI, J., AKAO, T., TANAKA, H., UENISHI, M., KIMURA, M. & OKAMOTO, T. (2002) Self-regeneration of a Pd-perovskite catalyst for automotive emissions control. *Nature,* 418.

PORTA, P., CIMINO, S., ROSSI, S. D., FATICANTI, M., MINELLI, G. & PETTITI, I. (2001) AFeO3 (A=La, Nd, Sm) and $LaFe_{1-x}Mg_xO_3$ perovskites: structural and redox properties. *Materials Chemistry and Physics,* 71**,** 165-173.

RIETVELD, H. M. (1969) A profile refinement method for nuclear and magnetic structures. *Journal of Applied Crystallography,* 2**,** 65.

ROZENBERG, G. K., PASTERNAK, M. P., XU, W. M., DUBROVINSKY, L. S., CARLSON, S. & TAYLOR, R. D. (2005) Consequences of pressure-instigated spin crossover in $RFeO_3$ perovskites; a volume collapse with no symmetrymodification. *Europhys. Lett.,* 71.

RUBIN, J., PIQUER, C., FILOTI, G., PARRA-BORDERIAS, M., BARTOLOME, F. & BARTOLOME, J. (2007) Mossbauer spectral study of $NdFe_{1-x}Ga_xO_3$ perovskites. *Journal of Magnetism and Magnetic Materials,* 316**,** e684-e687.

SANGALETTI, L., DEPERO, L. E., ALLIERI, B., NUNZIANTE, P. & TRAVERSA, E. (2001) An X-ray study of the trimetallic $La_xSm_{1-x}F_eO_3$ orthoferrites. *Journal of the European Ceramic Society,* 21.

SINGH, M. K., JANG, H. M., GUPTA, H. C. & KATIYAR, R. S. (2008) Polarized Raman scattering and latttice eigenmodes of antiferromagnetic $NdFeO_3$. *Journal of Raman Specrtoscopy,* 39.

STEVENSON, J. W., ARMSTRONG, T. R., CARNEIN, R. D., PEDERSON, L. D. & WEBA, W. J. (1996) *Journal of Electrochem. Soc.,* 143.

TOKURA, Y. (2007) Multiferroics - toward strong coupling between magnetization and polarization in a solid. *Journal of Magnetism and Magnetic Materials,* 310.

TRAVERSA, E., NUNZIANTE, P., SANGALETTI, L., ALLIERI, B., DEPERO, L. E., AONO, H. & SADAOKA, Y. (2000) Synthesis and Structural Characterization of Trimettallic Perovskite-Type Rare-Earth Orthoferrites, $La_xSm_{1-x}FeO_3$. *J. Am. Ceram. Soc.,* 83.

TREVES, D. (1965) Studies of Orthoferrites at the Weizmann Institute of Science. *Journal of Applied Physics,* 36**,** 1033-1039.

WANG, W., XU, D. & SU, W. (2005) Raman Shift of $RMnO_3$ (R=La, Pr, Nd, Sm) Manganites. Chin. Phys. Lett., 22.